

Development of Coherent Raman Microscopy
for Characterization of Dairy Products
Master's Thesis

author:
Brian Bjarke Jensen
brjen12@student.sdu.dk

supervisor:
Jonathan R. Brewer
brewer@sdu.dk

January 1st, 2018

Contents

1	Introduction	1
2	Theory	3
2.1	Optical Interaction with Matter	3
2.2	Raman Spectroscopy	4
2.3	Stimulated Raman Spectroscopy	7
2.4	Methods of Detection	9
2.5	Lock-in Amplification	12
2.6	Butter as a Biophysical System	14
2.7	Effect of Salt on Raman Spectrum of Water	16
3	Materials and Methods	19
3.1	SRS Microscope	19
3.1.1	Laser and Optical Parameter Oscillator	19
3.1.2	Scanhead	20
3.1.3	Reference Signal Amplifier	21
3.1.4	Lock-in Amplifier	21
3.1.5	SRS Detector and Bias	22
3.2	Aqueous Solutions of Ions	23
3.3	Samples of Butter	24
3.4	Matlab Dataanalysis	25
3.4.1	Calibration to Signals from Aqueous Solutions of Ions	25
3.4.2	Determining Concentration of Ions in Butter	26
4	Results	27
4.1	SRS Microscope	27
4.1.1	Detector and Bias	27
4.1.2	Reference Signal Amplifier	31
4.1.3	Lock-in Amplifier	33
4.1.4	Imaging with SRS Microscope	34
4.2	Calibration of Signal at Varying Concentrations of Salt	36
4.3	Butter	40
5	Discussion	53
5.1	SRS Microscope	53
5.2	Dataanalysis and Calibration	54
5.3	Butter	55

6 Conclusion	59
Bibliography	61
7 Appendix	63
7.1 Appendix I	63
7.2 Protocol: Imaging of Aqueous Solutions of Ions for Calibration .	68
7.2.1 Datastructure and Filenaming	68
7.2.2 Imaging	68
7.3 Protocol: Imaging of Butter for Calculation of Concentration of Salt	69
7.3.1 Datastructure and Filenaming	69
7.3.2 Imaging	69
7.4 Script: Dataanalysis in Matlab for Calibration of Intensity of Raman Signal for Aqueous Solutions of Ions	69
7.5 Script: Dataanalysis in Matlab for Calculation of Concentration of Salt in Butter	81

Abstract

Stimulated Raman scattering (SRS) microscopy is predicted to be capable of producing images of greater quality than coherent anti-Stokes Raman scattering (CARS) microscopy. As no commercial solutions are available yet, it was attempted to create a microscope capable of acquiring images through the use of SRS and use this technique, along with the more common CARS-technique, to obtain and compare images of a variety of samples of butter. The images would then be analyzed using an automated script that is able to characterize the butter. The microscope was built and the parts were characterized, though it was not possible to make the microscope produce useful images within the timespan of the project. Using another microscope it was possible to acquire CARS-images and develop a automatic script that can detect and analyze droplets of water in images of butter. Furthermore the script is able to derive the concentration of NaCl within a sample of butter, while also providing information about the distribution of size as well as concentration of NaCl in individual droplets of water.

Acknowledgements

I want to thank my supervisor, Jonathan, for his persistence, competent guidance and for offering me to work on this exciting project. I also owe a big "thank you" to Danny Kyrping from the FKF workshop, for his dedicated help and his skilled craftsmanship, without whom this project would have never got as far as it is today. I want to thank Torben Christensen from the BMB workshop for his help machining parts for the microscope, and my fellow students Irina and Mette for their support and help during our study together. I also want to thank my friends Jeppe, Kristian and Brian for their support and cheerful attitudes while working together during the late nights at the university. Finally, I want to thank my family. Without them I would not have been where I am today. I dedicate my work to my parents.

"We stand on the shoulders of those who came before us."

Chapter 1

Introduction

Microscopy is a powerful scientific tool and has contributed to innumerable advancements. By introduction of fluorophores into classical light microscopy, it became possible to target specific species in an image, effectively increasing the amount of information that is gained from an image [1]. Over time, more techniques were developed, pushing the limits for the amount of information that could be obtained from an image. As new techniques were developed, the demand evolved as well. The use of fluorophores demanded that they were added to a sample prior to imaging. When in contact with a sample, the fluorophore may interfere and affect the measurements, which was realized when trying to image species much smaller than the fluorophore itself.

To overcome the need for a fluorophore, different microscopy techniques related to Raman scattering were developed. The microscopy techniques derived from coherent Raman scattering (CRS) allow for a label-free, noninvasive and chemical bond specific imaging of a sample, again increasing the effective amount of information that could be obtained from a sample. The CRS microscopy makes it possible to obtain images of biological specimens and tissue [2, 3, 4, 5], even at video-rate [6], and works by two fields of light (pump and Stokes) interacting to drive a vibrational mode that increases the rate at which Raman scattering occurs in a material.

One of the CRS techniques is known as coherent anti-Stokes Raman scattering (CARS) and yields an intensity in signal that is proportional to the squared intensity of the pump-laser. The images acquired using this technique has the advantages of CRS, but suffers from a constant background. The intensity of the signal exhibits a quadratic dependence on the pump-laser as well as the number of scatterers, which makes deconvolution of images obtained with CARS increasingly complex. Another technique that has the advantages of CRS is known as stimulated Raman scattering (SRS), which features a linear relation between intensity of signal and intensity of laser and number of scatterers. Furthermore, images obtained using the SRS-technique do not suffer from a constant background, yet a commercial SRS-system has still to become available.

The advantages offered by CRS-techniques makes it an obvious choice when investigating complex biological samples such as cancer-tissue, skin and even food-products. The plentiful amount of close packed CH-bonds in lipids, and OH-bonds in water allow for an intense CRS-signal to be created, making the technique ideal to obtain images of these types of samples. This project will

make an attempt at developing a microscope that is capable of creating images using not only fluorescence, but also CARS and SRS. To compare the capabilities of the SRS-technique with the well-known CARS-technique, images of butter will be acquired using both SRS and CARS.

To recognize the importance of automated data analysis and interpretation of data - as the amount of information obtained for an image is ever increasing - the project will also focus on developing an automatic routine to characterize the samples of butter that are analyzed. An automated analysis of a product has many benefits, one being the reduced amount of time between measurement and result. This is of interest to the industry, as it allows for easy quality control as well as collection of knowledge that may lead to an improvement of the product. This analysis will be built around the fact that the introduction of ions to water changes the Raman spectrum of the water [7, 8, 9]. By identifying wavenumbers of water, that change intensity on addition of NaCl, it will be attempted to infer the concentration of NaCl within the samples of butter from the concentration of NaCl in the droplets of water in butter. Furthermore the project will attempt to characterize the samples of butter structurally by interpreting the results obtained from the samples of butter.

Chapter 2

Theory

In this chapter the basis for Raman spectroscopy will be introduced through a classical physics-approach, leading to the theory used to understand SRS and CARS. Hereafter the functionality of the lock-in amplifier and the system used for detection will be described. Finally will be given a brief introduction to the samples of butter as well as the theory behind the method developed to determine the concentration of salt in butter. The theory related to Raman-effects is mainly based on "Coherent Raman Scattering Microscopy" by Xie [10].

2.1 Optical Interaction with Matter

The classical approach to describing optical interaction with matter provides only a qualitative description of the processes that make up the foundation of CRS, as the classical approach fails to recognize the quantized nature of the nuclear oscillations. A more in depth description can be obtained through a semi-classical or quantum-mechanical approach, though this is beyond the scope of this project. In classical physics, light is described as an electromagnetic wave, consisting of a magnetic and electric field. The electric field can be described by two perpendicular vectors - the real and the imaginary - both located in the plane that is perpendicular to the direction of propagation of the wave. The two vectors are used to describe the polarization of the electromagnetic wave.

The fluctuations in the electric field of the light-waves can be regarded as a periodic varying external field, when passing through matter. This varying field will give rise to a displacement of the electrons from their equilibrium positions in the matter; hence an induced electric dipole is created. The dipole moment created by a displacement r of a charge $-e$ can be described as shown in (2.1).

$$\mu(t) = -e \cdot r(t) \tag{2.1}$$

By summation over all N dipoles per unit volume of matter, the macroscopic polarization can be determined as shown in (2.2).

$$P(t) = N \cdot \mu(t) \tag{2.2}$$

When the electric field is weak compared to the field that binds the electron to the nucleus, the displacement of the electron can be considered proportional to the electric field E ; hence the polarization can be expressed in terms of the electric permittivity in vacuum and the susceptibility χ of the matter, as shown in (2.3).

$$P(t) = \epsilon_0 \chi E(t) \quad (2.3)$$

In modern laser microscopy, the peak light intensity in the focal volume easily reaches very high intensities. An estimation of the peak light intensity achieved in this system can be made, when it is known that the pulse length and frequency of the laser is 6ps and 80MHz. The average light intensity may be estimated to 1W within the sample. The energy in one pulse of light is calculated in (2.4).

$$\begin{aligned} \frac{1\text{W}}{80 \times 10^6 \text{Hz}} &= 1.25 \times 10^{-8} \text{W} \cdot \text{s} \\ \frac{1.25 \times 10^{-8} \text{W} \cdot \text{s}}{6 \times 10^{-12} \text{s}} &= 2.08 \times 10^3 \text{W} \end{aligned} \quad (2.4)$$

When the light is focused to a very small point (around $300\text{nm} \times 300\text{nm}$ for this system), the intensity per area of sample can be estimated. This is shown in (2.5).

$$\frac{2.08 \times 10^3 \text{W}}{9 \times 10^{-14} \text{nm}^2} = 2.31 \times 10^{16} \text{W} \cdot \text{nm}^{-2} \quad (2.5)$$

The intensity calculated in (2.5) induces a very strong electric field in any matter that the light passes through, resulting in a strong displacement of the electrons. When far from the equilibrium position the binding potential can no longer be assumed to be harmonic; hence in this case, the dependence between the electric field and the polarization of the matter is no longer linear. The contributions from the anharmonic displacement of electrons are small relative to the harmonic contributions and the potential may be described using a power series, as shown in (2.6).

$$\begin{aligned} P(t) &= \epsilon_0 \left[\chi^{(1)} E(t) + \chi^{(2)} E^2(t) + \dots + \chi^{(n)} E^n(t) \right] \\ &= P^{(1)}(t) + P^{(2)}(t) + \dots + P^{(n)}(t) \end{aligned} \quad (2.6)$$

Where n denotes the order of the contribution.

2.2 Raman Spectroscopy

All matter consists of atoms. The matter may be an inhomogenous mix of atoms arranged relative to each other as molecules. The arrangement of atoms into a molecular structure dictates how the atoms are able to move, relative to each other. This gives rise to a plethora of different rotational, vibrational and

electronic states of even a simple molecule. These states are commonly referred to as *rovibronic* states.

Most light that interacts with matter is scattered through the elastic Rayleigh scattering, though it was discovered by Sir C. V. Raman around 1928 that a small fraction of light - about one photon out of ten million - is scattered inelastically [11]. The change in energy of the inelastically scattered photons was later shown to correspond to transitions in the molecular rovibronic states of the matter.

Atoms consist of a nucleus and a number of electrons that are being held together by potential energy. Therefore, the motion of the electron is - to some extent - dictated by the motion of its nucleus. The electronic polarizability of the molecule is influenced by the presence of nuclear modes in the molecule. Assuming that the driving frequency of the electric field is far from any electronic resonance of the molecule, the induced dipole moment can be expressed in terms of the polarizability α and the electric field E , as shown in (2.7).

$$\mu(t) = \alpha(t)E(t) \quad (2.7)$$

By imagining that no nuclear modes or nonlinearities affect the polarizability, it can be approximated as a constant α_0 . When taking into account that nuclear modes do exist, it has been shown by Placzek [12] that the polarizability can be expressed in terms of the nuclear coordinate Q and expanded with a Taylor-series, as shown in (2.8).

$$\alpha(t) = \alpha_0 + \left(\frac{\delta\alpha}{\delta Q} \right)_0 Q(t) + \dots \quad (2.8)$$

The motion of the nucleus can be approximated as a classical harmonic oscillator, as shown in (2.9), which can be rewritten using Euler's formula to (2.10).

$$Q(t) = 2Q_0 \cos(\omega_v t + \phi) \quad (2.9)$$

$$Q(t) = Q_0 [e^{i\omega_v t + i\phi} + e^{-i\omega_v t - i\phi}] \quad (2.10)$$

Where Q_0 is the amplitude of the motion, ω_v is the resonance frequency of the nucleus and ϕ is the phase. The electrical field created by an incident field of light oscillating at ω_1 can be described as (2.11).

$$E(t) = Ae^{-i\omega_1 t} + c.c. \quad (2.11)$$

Combining equations (2.8),(2.10) and (2.11), the dipole moment (2.7) can be rewritten as (2.12).

$$\begin{aligned} \mu(t) &= (Ae^{-i\omega_1 t} + c.c.) \left(\alpha_0 + \left(\frac{\delta\alpha}{\delta Q} \right)_0 Q_0 [e^{i\omega_v t + i\phi} + e^{-i\omega_v t - i\phi}] \right) \\ \mu(t) &= \alpha_0 Ae^{-i\omega_1 t} + A \left(\frac{\delta\alpha}{\delta Q} \right)_0 Q_0 [e^{-i(\omega_1 - \omega_v)t + i\phi} + e^{-i(\omega_1 + \omega_v)t - i\phi}] + c.c. \end{aligned} \quad (2.12)$$

Where the first term on the right hand side describes the elastic Rayleigh-scattering - the frequency ω_1 is preserved. The second term describes the in-elastic Raman-shifted frequencies: Stokes ($\omega_1 - \omega_v$) and anti-Stokes ($\omega_1 + \omega_v$).

The electric field of the dipole oscillating at either the Stokes or the anti-Stokes frequency can be described using electrodynamics. For the Stokes frequency $\omega_s = \omega_1 - \omega_v$, the amplitude of the far field at a distance \mathbf{r} can be described as shown in (2.13).

$$E(\omega_s) = \frac{\omega_s^2}{4\pi\epsilon_0c^2} |\mu(\omega_s)| \frac{e^{ikr}}{r} \sin(\Theta) \quad (2.13)$$

Where k is the wave-vector of the field, c is the speed of light, Θ is the angle relative to the dipole axis and $|\mu(\omega_s)|$ is the amplitude of the dipole oscillation at the Stokes frequency. The energy flux along \mathbf{r} can be determined using the time-averaged Poynting flux, as shown in (2.14).

$$S(\omega_s) = \frac{\epsilon_0c}{2} |E(\omega_s)|^2 \quad (2.14)$$

From (2.14) it is possible to determine the total energy radiated per dipole by integrating over the unit sphere, as shown in (2.15).

$$I(\omega_s) = \frac{\epsilon_0c}{2} \left| \frac{\omega_s^2}{4\pi\epsilon_0c^2} \right|^2 \int_0^{2\pi} \left| |\mu(\omega_s)| \frac{e^{ikr}}{r} \sin(\Theta) \right|^2 d\Theta \quad (2.15)$$

Inserting (2.12) into (2.15), reveals (2.16).

$$I(\omega_s) = \frac{\omega_s^4}{12\pi\epsilon_0c^3} Q_0^2 |A|^2 \left| \frac{\delta\alpha}{\delta Q} \right|^2 \quad (2.16)$$

From (2.16) it can be seen how the model predicts a ω^4 dependence of the intensity of the Raman scattered light. Furthermore, the intensity scales with the intensity of the incident field $I_0 = |A|^2$ as well as the coupling between polarizability and the nuclear coordinate $\left| \frac{\delta\alpha}{\delta Q} \right|^2$.

The Raman scattering signal strength can also be defined using an analogue to Lambert-Beer's law, as shown in (2.17).

$$I(\omega_s) = Nz\sigma(\omega_s)I_0 \quad (2.17)$$

Where N is the number density of scatterers, z is the length of the path that the light takes through the sample, I_0 is the intensity of the incident field and σ is the Raman cross section. To further clarify the process, a visual representation of the Rayleigh and spontaneous Raman-scattering is shown in figure 2.1.

Rayleigh scattering is shown in the left part of figure 2.1, which shows how a pump photon (green) is absorbed by the material, that is then excited from the ground state and into a virtual state. Immediately after this, the material relaxed by emitting a photon with similar energy and frequency. Spontaneous Raman scattering is shown to the right, where a pump photon is absorbed, after which a Raman-scattered Stokes-shifted photon is emitted.

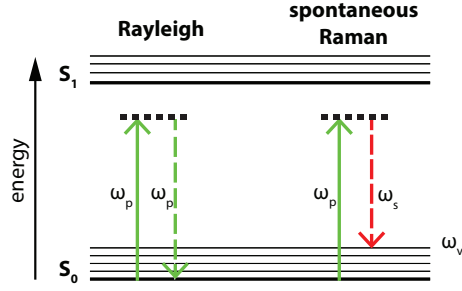


Figure 2.1: Energy diagram of the Rayleigh and spontaneous Raman scattering processes. Horizontal full bold lines show the ground state S_0 and first excited state S_1 of a material in which the Raman effect can occur. The relative positions of states indicate an increase in energy of the matter towards the top of the figure. The thin full lines represent vibrational states, while the dashed bold lines represent virtual states (rotational and electronic states have been omitted). Colored arrows represent photons, either being absorbed to increase the energy of the material (upward-facing arrows) or being emitted to lower the energy of the material (downward-facing dashed arrows). The color (and length) of each arrow indicates the relative energy, based on the visible spectrum of light.

2.3 Stimulated Raman Spectroscopy

The occurrence of Raman scattering is increased greatly by driving the nuclear mode of a system into resonance. This can be done by subjecting the system to two different fields of light E_1 and E_2 , where the difference in angular frequencies of the fields match up with a resonance frequency ω_v of the system. Both fields of light can be described as shown in (2.18).

$$E_i(t) = A_i e^{-i\omega_i t} + c.c. \quad (2.18)$$

As $\omega_1 > \omega_2 \gg \omega_v$, the nuclear mode of the system is not efficiently driven by the fields. Instead, the electrons are able to follow adiabatically. When the fields become intense enough, nonlinear electron motion can occur at combination frequencies such as $\Omega = \omega_1 - \omega_2$. Under these conditions, the combined field affects the nuclear vibrational oscillator with a force, as shown in (2.19).

$$F(t) = \left(\frac{\delta\alpha}{\delta Q} \right)_0 [A_1 A_2^* e^{-i\Omega t} + c.c.] \quad (2.19)$$

From (2.19) it can be seen that the electronic motions are coupled to the nuclear motions; hence the modulated electron cloud gives rise to a time-varying force oscillating at the frequency Ω . In the presence of the driving fields, the nuclear displacement can be described as shown in (2.20).

$$\frac{d^2 Q(t)}{dt^2} + 2\gamma \frac{dQ(t)}{dt} + \omega_v Q(t) = \frac{F(t)}{m} \quad (2.20)$$

Where γ is the damping constant and m the reduced mass. From (2.20) it is possible to determine the time-varying nuclear displacement as well as the amplitude expressed in terms of Ω , as shown in (2.21).

$$Q(t) = Q(\Omega)e^{-i\Omega t} + c.c.$$

$$Q(\omega_v) = \frac{1}{m} \left(\frac{\delta\alpha}{\delta Q} \right)_0 \frac{A_1 A_2^*}{\omega_v^2 - \Omega^2 - 2i\Omega\gamma} \quad (2.21)$$

From (2.21) it can be seen that the amplitude of the nuclear motion is largest when $\Omega = \omega_v$. It is also seen that the nuclear mode is driven by the combined action of the fields, and that the amplitude of the vibrational motion is dependent on the amplitude of the combined fields as well as the magnitude of the coupling between the nuclear coordinate and the electronic polarizability.

When the nuclear motion is driven by the fields, the optical properties of the material changes. Therefore, the electric fields E_1 and E_2 will experience slightly altered polarizability when traveling through the material. The macroscopic polarization can be described as a sum of the dipole moments, as shown in (2.22).

$$P(t) = N \left[\alpha_0 + \left(\frac{\delta\alpha}{\delta Q} \right)_0 Q(t) \right] [E_1(t) + E_2(t)] \quad (2.22)$$

Where the terms proportional to $\left(\frac{\delta\alpha}{\delta Q} \right)_0$ describes the contribution to the nonlinear polarization arising from the driven Raman mode. The nonlinear polarization can be expressed as shown in (2.23).

$$P_{NL}(t) = P(\omega_{cs})e^{-i\omega_{cs}t} + P(\omega_2)e^{-i\omega_2t} + P(\omega_1)e^{-i\omega_1t} + P(\omega_{as})e^{-i\omega_{as}t} + c.c. \quad (2.23)$$

Where $\omega_{cs} \equiv 2\omega_2 - \omega_1$ is the coherent Stokes frequency and $\omega_{as} \equiv 2\omega_1 - \omega_2$ is the anti-Stokes frequency. Therefore, the nonlinear contributions consist of four different frequencies; the two fundamental frequencies ω_1 and ω_2 , as well as the new frequencies ω_{cs} and ω_{as} . The amplitude of the polarization at these frequencies can be determined as shown in (2.24) through (2.27).

$$P(\omega_{as}) = \frac{N}{m} \left(\frac{\delta\alpha}{\delta Q} \right)_0^2 \frac{A_1^2 A_2^*}{\omega_v^2 - \Omega^2 - 2i\Omega\gamma} = 6\epsilon_0 \chi_{NL}(\Omega) A_1^2 A_2^* \quad (2.24)$$

$$P(\omega_{cs}) = 6\epsilon_0 \chi_{NL}^*(\Omega) A_1^* A_2^2 \quad (2.25)$$

$$P(\omega_2) = 6\epsilon_0 \chi_{NL}^*(\Omega) |A_1|^2 A_2 \quad (2.26)$$

$$P(\omega_1) = 6\epsilon_0 \chi_{NL}(\Omega) A_1 |A_2|^2 \quad (2.27)$$

Where the nonlinear susceptibility is given as shown in (2.28). The susceptibility is a tensor that describes the interaction between the matter and the four different fields.

$$\chi_{NL}(\Omega) = \frac{N}{6m\epsilon_0} \left(\frac{\delta\alpha}{\delta Q} \right)_0^2 \frac{1}{\omega_v^2 - \Omega^2 - 2i\Omega\gamma} \quad (2.28)$$

The four different frequencies correspond to the lower order coherent Raman effects: coherent anti-Stokes Raman scattering (CARS) and coherent Stokes Raman scattering (CSRS), as well as stimulated Raman gain (SRG) and stimulated Raman loss (SRL). To clarify the process, a sketch of the energy diagram of the SRS and CARS processes is shown in figure 2.2.

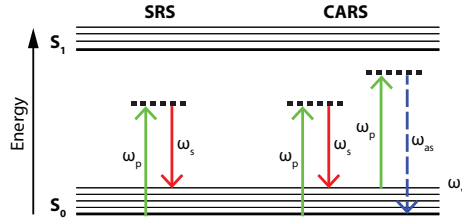


Figure 2.2: Energy diagram of the SRS and CARS processes. Colored full-line arrows represent photons interacting with the material, while a dashed line represent an emitted photon. The color (and length) of each arrow indicate the relative energy, based on the visible spectrum of light.

From figure 2.2 it can be seen for the SRS, how a pump and a Stokes-photon act together to bring the material into the a higher vibrational state. Under these conditions stimulated Raman scattering occurs. Furthermore it can be seen for the CARS, how - under conditions that allow for stimulated Raman scattering - a pump-photon is absorbed, after which the material emits an anti-Stokes photon and relaxes back to the ground state.

2.4 Methods of Detection

It is possible to describe how the energy flows between the different fields of light, as well as the matter. This can be done by evaluating Maxwell's wave equation, while taking all four different frequencies of the lower order coherent Raman effects into account. This is, however, beyond the scope of this project and therefore the topic will only be described qualitatively.

Due to the incident fields of light and the lower order coherent Raman-effects, two ways of detection exist: homodyne (detection of radiation from only one field) and heterodyne (detection of radiation from two or more fields). Detection of the CSRS and CARS signals at ω_{cs} and ω_{as} are homodyne, while detection of the SRL and SRG at ω_1 and ω_2 are heterodyne. This is due to the incident fields that radiate at the same frequencies as the signal. As an initial approach, the homodyne detection of CARS can be described by considering the non-linear field and intensity, as shown in (2.29) and (2.30).

$$E_{as}^{(3)}(t) = A_{as}e^{-i\omega_{as}t} + c.c. \quad (2.29)$$

$$I(\omega_{as}) = \frac{\epsilon_0 c}{2} |A_{as}|^2 \quad (2.30)$$

When considering only the lowest order of coherent Raman interactions, the only source for the anti-Stokes field is the nonlinear polarization that oscillates at ω_{as} . Therefore, the magnitude of the anti-Stokes field A_{as} is proportional to the magnitude of $P(\omega_{as})$. From (2.24) it is possible to deduce (2.31).

$$I(\omega_{as}) \propto |\chi_{NL}|^2 I_1^2 I_2 \quad (2.31)$$

From (2.31) it can be seen that the intensity of the CARS-signal is quadratically proportional to both the intensity of the field at ω_1 as well as the number of Raman-scatterers N (seen from (2.28)). Furthermore it can be seen that the process of mixing between the fields oscillating at ω_1 and ω_2 to create the field at ω_{as} is parametric, as no energy has been exchanged with the material.

This is, however, not the case in the presence of yet another field: a local oscillator that is created by Raman-scattering. Upon addition of the local oscillator which has the same phase as the nonlinear polarization, the induced nonlinear polarization is no longer the only source of radiation at the signal frequency ω_{as} . The intensity in the anti-Stokes frequency channel at the detector can therefore be described as (2.32).

$$\begin{aligned} I(\omega_{as}) &= \frac{\epsilon_0 c}{2} \left| E_{as}^{(3)} + E_{as}^{lo} \right|^2 \\ &\propto \left| E_{as}^{(3)} \right|^2 + \left| E_{as}^{lo} \right|^2 + \left[\left(\left| E_{as}^{(3)} \right|^2 \right)^* \left| E_{as}^{lo} \right|^2 + \left(\left| E_{as}^{lo} \right|^2 \right)^* \left| E_{as}^{(3)} \right|^2 \right] \end{aligned} \quad (2.32)$$

Where E_{as}^{lo} is the local oscillator field at the anti-Stokes frequency. The right-most term in (2.32) is describing contribution by the heterodyne¹ mixing, which is seen to depend both on the nonlinear anti-Stokes field and the local oscillating field. The heterodyne contribution can be rewritten as (2.33).

$$\begin{aligned} I_{het}(\omega_{as}) &= 2A_{as}^{lo} \left[Re \left\{ E_{as}^{(3)} \right\} \cos(\phi) + Im \left\{ E_{as}^{(3)} \right\} \sin(\phi) \right] \\ &= 2\alpha \left[Re \{ \chi_{NL} \} \cos(\phi - \phi_p) + Im \{ \chi_{NL} \} \sin(\phi - \phi_p) \right] \end{aligned} \quad (2.33)$$

Where $\alpha = |A_{as}^{lo} A_1^2 A_2|$, A_{as}^{lo} is the amplitude of the local oscillator (at the anti-Stokes frequency), ϕ is the phase difference between the fields $E_{as}^{(3)}$ and E_{as}^{lo} and ϕ_p is the phase difference between $E_{as}^{(3)}$ and $P(\omega_{as})$. A short overview of the implications of different interesting values of $\Delta\phi$ is shown in table 2.1.

As the imaginary part of the heterodyne contribution of (2.33) becomes greater than zero, the process is seen to no longer be purely parametric and dissipative interactions will grow in significance as they scale with $Im(\chi_{NL})$. Modulation techniques can be applied to measure the effect of the dissipative interactions, which is how SRS is made possible.

It is interesting to consider the case where the local oscillator is driven at the vibrational resonance frequency $\Omega = \omega_v$. Under these conditions, it can be seen from (2.28) that the susceptibility becomes imaginary, when nonresonant contributions are ignored. The total intensity detected in the anti-Stokes channel can then be described as (2.34).

¹Heterodyne detection is done at a field mode that is already occupied (for SRL it is ω_1), while homodyne is detection at a field mode that is initially vacant (e.g. CARS at ω_{as}).

$\Delta\phi$	effect
0	heterodyne term disappears; total detected energy from homodyne contributions only
$-\frac{\pi}{2}$	heterodyne term becomes negative; total detected energy in channel is less than sum of homodyne contributions
$\frac{\pi}{2}$	heterodyne term becomes positive; total detected energy in channel is greater than sum of homodyne contributions

Table 2.1: Implications of different values of $\Delta\phi$ on intensity of signal in ω_{as} channel.

$$I(\omega_{as}) \propto |E_{as}^{(3)}|^2 + |E_{as}^{lo}|^2 + 2\alpha \text{Im} \{ \chi_{NL} \} \sin(\phi - \phi_p) \quad (2.34)$$

From (2.34) it can be seen how the intensity of the detected signal depends on the phase difference $\Delta\phi = \phi - \phi_p$. Therefore it can be understood that the presence of a local oscillator can change the sensitivity of the measurement, when probing parametric and dissipative processes. The phase difference can be described in greater detail by more elaborate theories, though this approach offers a description of the mixing between fields that is adequate to reach an intuitive understanding of the subject - which is what is needed to construct the SRS microscope.

Regarding the intensity of the SRL signal, the incident and the nonlinear fields oscillate at the same frequency and will therefore interfere with each other. The incident field can be considered as a local oscillator, while using the same approach as before, the total intensity in the channel can be described as (2.35).

$$I(\omega_1) = \frac{\epsilon_0 c}{2} |E_1^{(3)} + E_1|^2 \\ \propto |E_1^{(3)}|^2 + |E_1|^2 + 2\beta [\text{Re} \{ \chi_{NL} \} \cos(\delta\phi) + \text{Im} \{ \chi_{NL} \} \sin(\delta\phi)] \quad (2.35)$$

Where $\beta = I_1 I_2$. It is known from the plane wave approximation that the phase shift $\Delta\phi$, in the far field is equal to $-\frac{\pi}{2}$; hence the real part of the susceptibility is $\frac{\pi}{2}$ retarded with respect to E_1 , while the imaginary part is out-of-phase. In this case, the intensity can be described as (2.36).

$$I(\omega_1) \propto |E_1^{(3)}|^2 + |E_1|^2 - 2\beta \text{Im} \{ \chi_{NL} \} \quad (2.36)$$

From (2.36) it can be seen how the total intensity at ω_1 is attenuated by the presence of the driven oscillator field (also radiating at $\omega_1 = \omega_2 + \omega_v$), which is caused by the nonlinear contribution from E_2 . As the amplitude of the field E_1 is proportional to the polarizability, using (2.27), the intensity at ω_1 can be described as shown in (2.37).

$$I(\omega_1) \propto \chi_{NL} I_1 I_2 \quad (2.37)$$

From (2.37) it can be seen how the intensity of the SRL-signal is proportional to both the intensity of the fields ω_1 and ω_2 as well as the number of Raman scatterers.

It can be concluded that the driven harmonic oscillator at the resonance frequency ω_v forms a material modulation, which affects the amplitude of the fundamental fields passing through the material. The material modulation allows for the Raman-scattering, which produces radiation at the Stokes ω_s and anti-Stokes ω_{as} frequencies, as well as at $\omega_1 - \omega_v$ and $\omega_2 + \omega_v$. The two latter field contributions radiate at the same frequencies as the fundamental fields E_i ; hence interaction between the nonlinear fields $E_i^{(3)}$ (caused by the other fundamental field) and the fundamental fields E_i will occur. The interaction gives rise to the loss and the gain in the ω_1 and ω_2 channels, respectively. Finally it can be concluded that the magnitude of the gain and loss is proportional to the imaginary part of the nonlinear susceptibility: the dissipative part.

2.5 Lock-in Amplification

This description of the lock-in technique is based on the detailed descriptions by [13, 14, 15]. A lock-in amplifier resembles an AC voltmeter, but has more features. As a normal AC voltmeter, the lock-in amplifier is able to measure the V_0 of the sinusoidal voltage V_{in} shown in (2.38).

$$V_{in}(t) = V_0 \sin(\omega_0 t + \Theta) \quad (2.38)$$

Where $\omega_0 = 2\pi f_0$ is the angular frequency, f_0 is the natural frequency and Θ is the phase. The lock-in features the ability to single out a change in voltage at a very narrow band of frequencies; hence ignoring all signals at other frequencies than what is provided at its reference input. A diagram of the functionality of the lock-in amplifier is shown in figure 2.3.

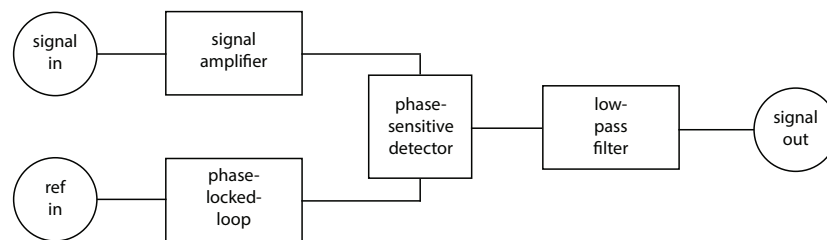


Figure 2.3: Diagram of the lock-in amplifier-functionality.

The phase-locked-loop (PLL), shown in figure 2.3, is an internal oscillator that is synchronized to the input-reference. The PLL creates its own signal to be used by the phase-sensitive detector (PSD), which is done in order to create a stable reference signal for each iteration in the PSD. The PSD works by multiplying the amplified input-signal by the PLL-signal; hence the output of the PSD is the product of the two AC-voltages V_{in} and V_{PLL} . This is shown in (2.39).

$$V_{PSD} = V_{in} \sin(\omega_{in} t + \Theta_{in}) V_{PLL} \sin(\omega_{PLL} t + \Theta_{PLL}) \quad (2.39)$$

The two AC-signals in (2.39) can be expanded as shown in (2.40).

$$\begin{aligned} V_{PSD} &= V_{in} V_{PLL} \frac{1}{2} \{ \cos[(\omega_{in} t + \Theta_{in}) - (\omega_{PLL} t + \Theta_{PLL})] \\ &\quad - \cos[(\omega_{in} t + \Theta_{in}) + (\omega_{PLL} t + \Theta_{PLL})] \} \\ V_{PSD} &= V_{in} V_{PLL} \frac{1}{2} \{ \cos[(\omega_{in} - \omega_{PLL})t + \Theta_{in} - \Theta_{PLL}] \\ &\quad - \cos[(\omega_{in} + \omega_{PLL})t + \Theta_{in} + \Theta_{PLL}] \} \end{aligned} \quad (2.40)$$

For the one case where the input- and reference-frequency are equal, (2.40) reduces to (2.41).

$$\begin{aligned} V_{PSD} &= V_{in} V_{PLL} \frac{1}{2} \{ \cos[\Theta_{in} - \Theta_{PLL}] \\ &\quad - \cos[(\omega_{in} + \omega_{PLL})t + \Theta_{in} + \Theta_{PLL}] \} \end{aligned} \quad (2.41)$$

The first term of (2.41) is now time-independent, which is equivalent to a DC-voltage; hence in this case, the output of the PSD is an AC-voltage with a DC-offset. At this point, the low pass filter (LPF) from figure 2.3 becomes crucial, as its sole purpose is to hinder the passage of any AC-components in the signal from the PSD!

The lowpass filter is described in detail in [14] and can be easily described in the frequency domain, where the relation between the incoming and the filtered signal is shown in (2.42).

$$Q_{out}(\omega) = H(\omega) Q_{in}(\omega) \quad (2.42)$$

Where $H(\omega)$ is the transfer function of the filter and $Q_{in}(\omega)$ and $Q_{out}(\omega)$ are the Fourier transforms of the respective signals in the time domain. As no perfect filters exist, a reasonable approximation of the transfer function can be made using the RC-filter model, where the function is described as shown in (2.43).

$$H(\omega) = \frac{1}{1 + i\omega\tau} \quad (2.43)$$

Where $\tau = RC$ is the filter time constant with R being the resistance and C the capacitance of the filter. A sketch of multiple LPFs connected in a series is shown in figure 2.4.

By cascading the filters as shown in figure 2.4 the order of the roll-off of the lock-in is increased. The transfer function can in this case be written as (2.44).

$$H_n(\omega) = H_1(\omega)^n = \left(\frac{1}{1 + i\omega\tau} \right)^n \quad (2.44)$$

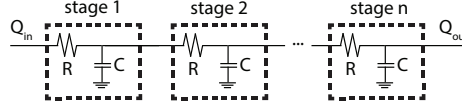


Figure 2.4: Sketch of the arrangement of components inside the LPF.

From equation (2.44) it can be seen how the attenuation of the signal that passes through a series of filters is related to the number n of (identical) filters it passes through. the number n is defined as the *order* of the filter; the higher the order, the narrower a bandwidth - around the provided reference-frequency - is allowed to pass through the filter.

Modern lock-in amplifiers are of the type *dual-phase lock-in* and feature at least one pair of PSDs. The pairing of the PSDs allow for the PLL to send one signal to one PSD and a $\frac{\pi}{2}$ phase-shifted signal to the other PSD. Therefore the output of the two PSDs can be described as shown in (2.45).

$$\begin{aligned} V_{PSD1} &\propto V_{in} \cos(\Theta_{in} - \Theta_{PLL}) \\ V_{PSD2} &\propto V_{in} \cos(\Theta_{in} - \Theta_{PLL} + \frac{\pi}{2}) = V_{in} \sin(\Theta_{in} - \Theta_{PLL}) \end{aligned} \quad (2.45)$$

As per tradition the outputs from the PSDs are defined as X and Y , where X is the *in-phase* component and Y the *quadrature* component. This is shown in (2.46).

$$\begin{aligned} X &= V_{in} \cos(\Theta_{in} - \Theta_{PLL}) \\ Y &= V_{in} \sin(\Theta_{in} - \Theta_{PLL}) \end{aligned} \quad (2.46)$$

The advantage of measuring both the in-phase and quadrature-component at the same time, is the possibility to directly derive the amplitude R and phase Θ of the signal vector. These quantities are calculated by transformation from Cartesian coordinates into polar coordinates, which is shown in (2.47).

$$\begin{aligned} R &= \sqrt{X^2 + Y^2} \\ \Theta &= \text{atan2}(Y, X) \end{aligned} \quad (2.47)$$

The use of *atan2* instead of *atan* allows Θ to cover all four quadrants: $(-\pi, \pi]$.

2.6 Butter as a Biophysical System

Butter is defined by FAO/WHO to contain 80w% milk fat and no more than 16w% water [16]. All samples of butter used in this project are initially produced as unsalted versions, to which a slurry of salt and water is added. Butter contain small amounts of other nutrients such as carbohydrates, proteins and salt. The fraction of water compared to lipid allows for the formation of a lipid matrix with water droplets embedded within. The distribution of the remaining constituents

is dictated mainly by the solubility; highly polar compounds are located within the polar water droplets, while apolar compounds are located in the apolar lipid matrix. Some compounds may even be situated at the interface between the apolar and polar compounds: amphiphiles such as emulsifiers and some proteins are examples hereof. An image of butter is shown in figure (2.5).

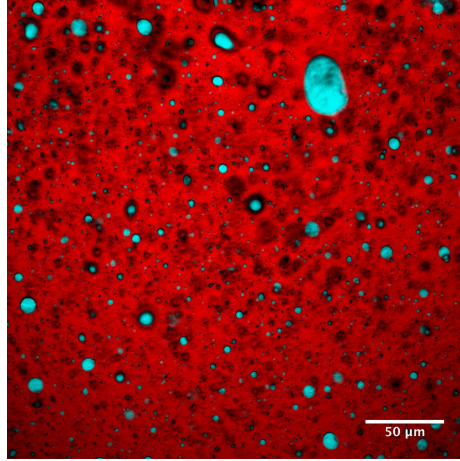


Figure 2.5: Image of butter. The image is a combination of two images: Blue: detected at 3185cm^{-1} (water). Red: detected at 2850cm^{-1} (lipid).

To estimate the concentration of salt (based on mass) in a sample of butter, the density of the constituents must be known. It is possible to estimate the concentration of salt in the butter, when the relative amount of constituents as well as the density of the butter are known. Upon dissolution, NaCl splits into Na^+ and Cl^- , which are charged ions and highly polar. It is reasonable to assume that all salt present in a sample of butter, is located within the water droplets; hence the concentration of salt in the sample of butter can be expressed from the concentration of salt in the droplets, as shown in (2.48).

$$\begin{aligned} c_{\text{sample}} \cdot \rho_{\text{butter}} \cdot V_{\text{butter}} &= c_{\text{droplets}} \cdot \rho_{\text{water}} \cdot V_{\text{droplets}} \\ c_{\text{sample}} &= \frac{c_{\text{droplets}} \cdot \rho_{\text{water}} \cdot V_{\text{droplets}}}{\rho_{\text{butter}} \cdot V_{\text{butter}}} \end{aligned} \quad (2.48)$$

Assuming that the butter is homogenously mixed and isotropic on a macroscopic scale, the volume of water per volume of sample is constant throughout the sample. Therefore a 2-dimensional slice of the sample is representative for the whole 3-dimensional sample and the droplet area per image area-fraction x can be written as shown in (2.49).

$$x_{\text{droplets/sample}} = \frac{V_{\text{droplets}}}{V_{\text{sample}}} = \frac{A_{\text{droplets}}}{A_{\text{sample}}} \quad (2.49)$$

Using (2.49), it is possible to rewrite (2.48), as shown in (2.50).

$$c_{\text{sample}} = \frac{c_{\text{droplets}} \cdot \rho_{\text{water}} \cdot x_{\text{droplets/sample}} \cdot V_{\text{butter}}}{\rho_{\text{butter}} \cdot V_{\text{butter}}}$$

$$c_{\text{sample}} = \frac{c_{\text{droplets}} \cdot \rho_{\text{water}} \cdot x_{\text{droplets/sample}}}{\rho_{\text{butter}}} \quad (2.50)$$

From (2.50) it is possible to calculate the concentration of salt in a sample of butter, based on the determined concentration of salt in the droplets as well as the droplets area per image area-fraction. The density of water is per definition $1\text{g} \cdot \text{cm}^{-3}$. The density of butter is given by Elert as $\rho_{\text{butter}} = 0.911\text{g} \cdot \text{cm}^{-3}$ [17], which is used when estimating the concentration of salt during the data analysis.

2.7 Effect of Salt on Raman Spectrum of Water

It has been shown by Hibben that molecules of water in the liquid phase, tend to arrange themselves relative to other water molecules in the same way as if the molecules were in the solid phase [7]. This relative arrangement is referred to as the *four-coordinated water molecule*. A sketch of the four-coordinated water molecule is shown in figure 2.6. This structure of the water molecule at 0°C was first suggested by J. D. Bernal and R. H. Fowler in 1933. It was later shown by Pauling that the four-coordinated water molecule is made up from an Oxygen-atom with two closely located Hydrogen-atoms - resembling the structure of an isolated water molecule - while the other two Hydrogen-atoms are located at a greater distance from the Oxygen-atom and probably are bound to Oxygen-atoms of other water molecules [18].

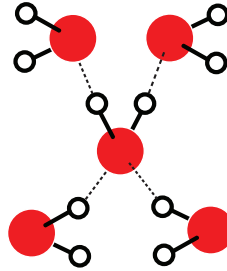


Figure 2.6: Sketch of the structure of four-coordinated water molecule.

The Raman spectrum of water has been studied and peaks in the spectrum have been suggested to be linked to degrees of intermolecular coordination between water molecules [7, 19, 20]. Furthermore the peaks in the $2700\text{--}3800\text{cm}^{-1}$ region have been proven to be related to OH stretching by Carey [8]. The measured Raman spectrum overlayed with a Gaussian deconvolution for this region is shown in figure 2.7.

It is clear from figure 2.7 that the relative intensity between two major local maxima around 3250cm^{-1} and 3400cm^{-1} would be affected by the addition of salts. The introduction of ions to the water would force water molecules to orient according to the charge of the ion; hence the overall coordination of water

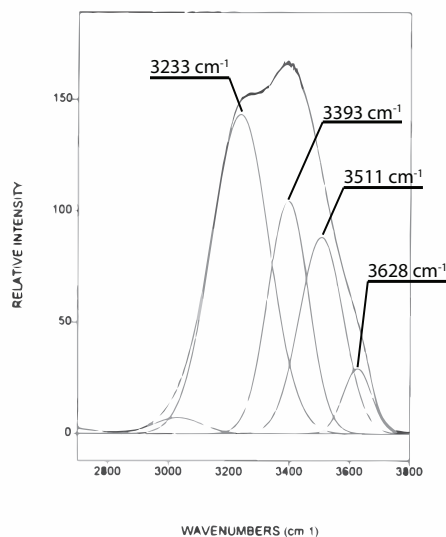


Figure 2.7: Raman spectrum of water (24°C, 128 bar) with Gaussian deconvolution overlaid. Modified from [8].

molecules will be shifted towards lower intermolecular coordination. Combined results from [19] and [8] are shown in table 2.2.

source of spectrum	coordination peak [cm ⁻¹]			
	4	3	2	1
ice (0°C, 1 bar) [19]	3150	3270	3390	..
water (24°C, 256 bar) [8]	3233	3393	3511	3628
water (40°C, 1 bar) [19]	3190	..	3440	3650

Table 2.2: Suggested coordination-numbers for discovered Raman peaks. N.B. all results from [19] are calculated based on an estimate of the position of the 4-coordinated peak.

The wavenumbers, of table 2.2 at which peaks related to different degrees of coordination of water molecules, suggest the possibility to determine the overall coordination of water molecules within a sample, based on the relative intensity of the deconvoluted peaks shown in figure 2.7. Instead of measuring the Raman spectrum of a sample - which takes relatively long time, due to the repeated tuning of the laser - the relative intensity between two wavenumbers may be used to estimate the degree of coordination. The Raman spectrum from figure 2.7 shows two distinctive peaks at approximately 3233cm⁻¹ and 3393cm⁻¹, which may be directly used to infer the relative coordination of water molecules. The relative intensity of the signal at the two peaks has been shown to change with the concentration of ions; hence it is possible to establish a relation between these, as shown by Durickovic [21].

Chapter 3

Materials and Methods

The following chapter describes the materials and methods used during this project. Initially the SRS microscope will be discussed, after which the samples of butter, calibration of the method used for determining salt in butter and the method itself is described.

3.1 SRS Microscope

The following section describes the components that are essential to the functioning of the SRS-microscope.

3.1.1 Laser and Optical Parameter Oscillator

The laser pumping the optical parameter oscillator (OPO) creates a beam of 1064nm laser light, which is pulsed at 80MHz with a pulselength of 6ps. The OPO is a picoEmerald (APE GmbH) and frequency-doubles the received laser to 532nm, from which it generates its two output-beams: *signal* and *idler*. The signal-beam is tunable within the range of 720 – 990nm, while the idler-beam is tunable within the range of 1150 – 2300nm. Furthermore the OPO passes some of the 1064nm laser, that it is pumped by. This is used as the Stokes-laser by the microscope system. The idler-beam is unused, while the signal-beam is used as the pump-laser, which is tuned to match a vibrational frequency that stimulates Raman scattering from a material being investigated. The vibrational frequency that is probed by illumination with the pump and the Stokes laser is calculated as shown in (3.1).

$$\nu_{vib} = \frac{1}{\lambda_{pump}} - \frac{1}{\lambda_{Stokes}} \quad (3.1)$$

The OPO can be set to modulate the Stokes beam at a frequency of 10MHz. This is done by entering the following commands (press buttons: *config*, *terminal*), one at a time, in the terminal controlling the OPO:

1. `expert=13053`
2. `:AOM:W:16:1:536870912`

3. :AOM:W:16:2:4

The electrical optical modulator (EOM) is now activated by pressing the buttons in the terminal: *config*, *modulator*, *EOM*. When the EOM-button is pressed in, the EOM is activated. The OPO features a port on the back, named *AOM SYNC*, from which the 10MHz reference signal is sent out. As is understood from the purpose, the modulator blocks half of the light. Therefore the average power of the modulated beam from the laser used in this setup can only reach around 600mW of power.

3.1.2 Scanhead

The scanhead, on the microscope being developed in this project, was not worked on or changed in any way, though it is an essential (and exciting) part to consider when doing microscopy - and deserves to be mentioned. Therefore the constituents and functioning of the scanhead is described in the following section. The scanhead is based on a design by Ding [22]. A sketch of the scanhead is shown in figure 3.1.

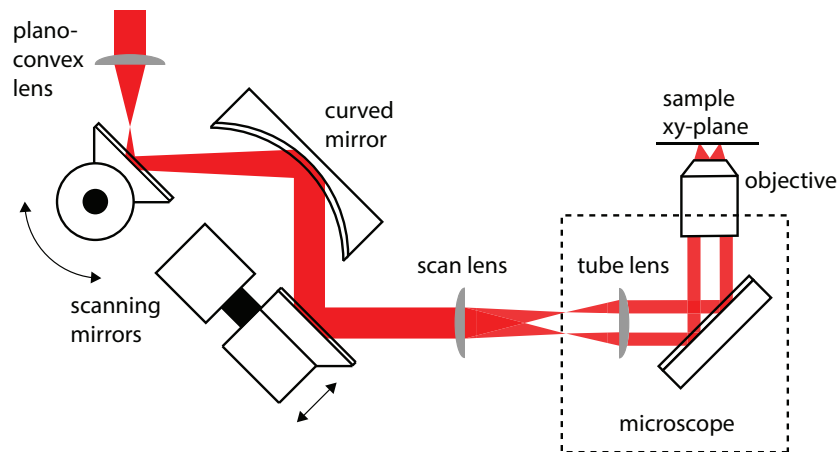


Figure 3.1: Sketch of the scanhead used in the SRS-microscope.

From figure 3.1 it can be seen how the curved mirror is used to project the image of the first scanning mirror onto the second scanning mirror. To counteract the focusing of the beam by the curved mirror, a planoconvex lens is placed before the first scanning mirror, ensuring that collimated light reaches the focal point of the scan lens. The scan lens and the tube lens work together to create an image of the first scanning mirror in the back-focal plane of the objective. By rotating the mirrors, the image of the light source can be moved around on the scan lens and therefore also in the back focal plane of the objective. This makes it possible to move the position of the focused beam in the sample xy-plane; hence the sample can be scanned, one point at a time by moving the mirrors accordingly.

3.1.3 Reference Signal Amplifier

A diagram of the instrument created to amplify the reference signal from the laser is shown in figure 3.2.

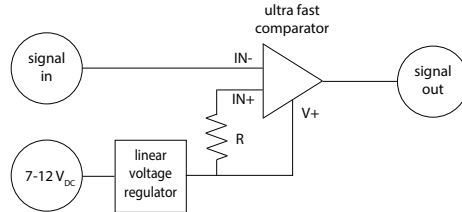


Figure 3.2: Diagram of the essential components used in the reference signal amplifier.

From figure 3.2 it can be seen how a static resistor is used to set the threshold of the comparator, based on the voltage delivered from the linear voltage regulator. The comparator is of the type *AD8611* and features a very small propagation delay of only 4ns, which is used to generate the amplified output signal.

3.1.4 Lock-in Amplifier

The lock-in amplifier used in this setup is the *eLockIn205/2* from Anafatec, for a full description of the instrument, please refer to [23]. The lock-in is digital with a 16-bit analog-to-digital input conversion, an operational bandwidth of dc to 10 MHz and three available roll-off settings: $6 \frac{\text{dB}}{\text{oct}}$, $12 \frac{\text{dB}}{\text{oct}}$ or $24 \frac{\text{dB}}{\text{oct}}$. The possible settings of roll-off are a result of how the lowpass filters are made. The roll-off setting simply adjust the order of roll-off filter used: 1st, 2nd or 4th order filters are available. The lock-in features a dynamic reserve of 135 dB (ability to detect a signal among noise that is $\sqrt{10^{\frac{135\text{dB}}{10}}} \approx 5.6 \times 10^6$ times greater than the signal). Furthermore it allows for dual input and quad-phase detection. This is shown in figure 3.3.

From figure 3.3 it can be seen that the *eLockIn205/2* features two inputs, each connected to two PSDs. The dual input may be utilized when the laser-intensity is not stable during the time it takes to acquire an image, to determine the difference in signal immediately. As the laser used in this setup is stable (only affected by relatively slow fluctuations in intensity as a result of thermal fluctuations), the single input is used for detection. The input impedance of the lock-in is $1\text{M}\Omega$. The preamplification stage shown in figure 3.3 is used to adjust the amplification of the analog signal, before it is converted to a digital one. By adjusting the *range* of the lock-in, the input is preamplified to match the full scale of the 16-bit analog-to-digital converter; hence maximal resolution of the signal is achieved. The possible settings are 10V, 1V and 0.1V, with maximum ratings at $\pm 3.6\text{V}_{\text{RMS}}$, $\pm 360\text{mV}_{\text{RMS}}$ and $\pm 35\text{mV}_{\text{RMS}}$ respectively. The lock-in also allows for sampling over a specified time-interval t . As the signal is averaged over the sampling time, a longer time results in a better signal-to-noise ratio (SNR).

The lock-in features four modes of operation, though the only mode of interest - for this project - is the *lock-in mode*; hence only this mode will be discussed.

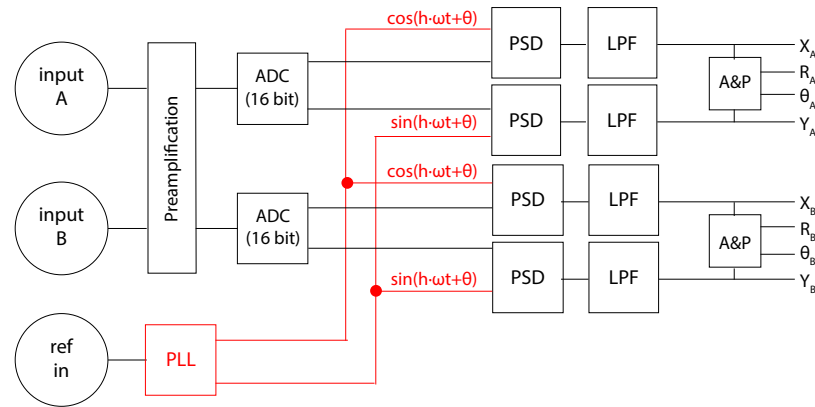


Figure 3.3: Full diagram of relevant components of the *eLockIn205/2* lock-in amplifier. The PLL connections have been marked with red.

In the lock-in mode, the screen of the instrument can be set to display a number of different values related to the functioning of the lock-in amplifier. On the back of the instrument are four ports named *display 1-4*, which per default output an analog signal (sampled at 1MHz) related to the values displayed on the screen in relative order. The range of the output scaling can be set manually in the lock-in amplifier, so that the values displayed on the screen are amplified to achieve maximal resolution in the analog ports.

Another port on the back of the instrument is the *ref in 1*-port, to which the reference frequency signal is connected. For the lock-in to function properly at 10MHz, the reference signal provided must be of the type *transistor-transistor logic* (TTL). This signal is defined as a logical signal; hence it indicates either a *zero* or a *one*. The logical zero or "low" is per definition perceived from a voltage of 0 – 0.8V, while the logical one or "high" is perceived from a voltage of 2 – 5V [24].

3.1.5 SRS Detector and Bias

The detector used in this setup is a large area anode-grounded Silicon-based photodiode (*SM1PD1B*, Thorlabs). The detector features a large active area (10 x 10 mm, behind Ø9 mm aperture), which allows for a better collection of light and is rated to work with a maximal bias of 25V. The detector works over a wide range of wavelength: 350nm to 1100nm. This is ideal for SRL, as the technique demands a larger range of responsivity, due to the tuning of the unmodulated pump laser. The detector is anode-grounded and produces a current-response when subjected to light. The current arising from shining light on the detector is converted to a negative voltage-response by placing a load resistor $R_L = 50\Omega$ between the detector and the lock-in amplifier.

The rise/fall time of the detector t_r can be estimated from the bandwidth of the detector f_{BW} by using (3.2).

$$f_{BW} = \frac{1}{2\pi R_L C_j} = 5.4\text{MHz}$$

$$t_r = \frac{0.35}{f_{BW}} \approx 65\text{ns} \quad (3.2)$$

Where the capacitance of the diode is $C_j \approx 590\text{pF}$ at 20V of bias. From (3.2) the rise/fall time is expected to be short enough for the detector to be able to distinguish the 100ns periods of the 10MHz modulation of the signal.

Furthermore the responsivity of the detector R_λ is defined as shown in (3.3).

$$R_\lambda = \frac{I_P}{P} \quad (3.3)$$

Where I_P is the current produced by the detector under the illumination by light with a power P . The responsivity is related to the wavelength of the incident light, which is described in greater detail in [25].

The bias used for the detector is a *PBM42* from Thorlabs. It features a female BNC connector towards the detector and a female SMA connector at its output. A 2.5 mm phono jack is used to provide the power for the bias. The diagram of the bias is shown in figure 3.4.

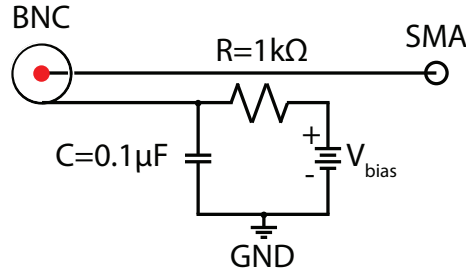


Figure 3.4: Diagram of the bias used for the detector.

The power supply for the bias is an *AC/DC switch mode plug-in* (12 – 30V model) from Mascot, which delivers maximally a 0.65A current. The power supply can be adjusted with a precision of $\pm 0.5\text{V}$.

To shield the detector from the modulated 1064nm laser, the optical filter *SRS-emitter HC 850/310* (AHF) was used.

3.2 Aqueous Solutions of Ions

To determine the relation of the signal from an aqueous solution of NaCl in relation to the concentration of NaCl, eight solutions of NaCl were prepared. It should be noted that it is not possible to solubilize more than approximately 35w% NaCl in pure water at 20°C (all experiments were conducted at room temperature). The salt needed for the correct concentration was determined by mass, after which it was transferred to a vial. Then 2 mL of Milli-Q water was added to the vial by a precision pipette. The solution was vortexed for 30 seconds to make sure that all salt had been solubilized.

Each sample was added to a well in a μ -Slide 8 Well Glass Bottom array (Ibidi GmbH) and was imaged using a 20x dry objective. All images were acquired at a depth of $100\mu\text{m}$ from the glass/water interface and two different wavenumbers were probed: $\nu_1 = 3180\text{cm}^{-1}$ and $\nu_2 = 3340\text{cm}^{-1}$. To ensure the quality of the measurements, all images were acquired five times with a line average of four. After five images, the laser was tuned for the other wavenumber and another five images were acquired. This was done five times for each wavenumber for all eight different concentrations of NaCl.

3.3 Samples of Butter

All samples of butter were stored at 5°C and imaged immediately after being mounted in the microscope to avoid melting of the sample. The samples were applied to a microscope slide ($1.0 - 1.2\text{mm}$, Fisherbrand) using a spatula and a cover glass ($\text{Ø } 25\text{mm}$, thickness no 1.5, VWR) was pressed gently down onto the sample. All samples were imaged using a 40x water-immersed objective.

The samples of butter that were investigated during this project are listed in table 3.1.

sample	$c_{\text{salt}}[\text{w}\%]$	comment
NS-1	1.2	normally salted butter
NS-2	1.2	normally salted butter
NS-3	1.2	normally salted butter,
NS-4	1.2	normally salted butter, organic
NS-5	1.2	normally salted butter, with 25% vegetable oil added
US	0	unsalted butter
HS	1.9	highly salted butter

Table 3.1: Table describing the different samples of butter - along with their concentrations of salt - that have been worked with, during this project. N.B. All samples of butter are from different lines of production.

All samples were imaged at five different locations within the sample, for both wavenumbers ν_1 and ν_2 . An xz-scan was used to determine the depth into the sample, at which the intensity was the greatest. This was found to be around $10\mu\text{m}$ from the glass/sample interface; hence images were acquired at this depth. The laser power was adjusted prior to acquiring the first image at the wavenumber ν_1 . This was done to achieve maximal intensity at the brightest wavenumber, without overloading the detectors. After this, the laser power was kept constant during imaging of the sample.

Furthermore two different model butter-systems were created: One system was made from coconut milk and the other from coconut oil. The systems were created to verify the ability of the data-analysis script to determine the concentration of NaCl correctly, as well as to investigate the behavior of simple and well defined butter-systems.

The system based on coconut milk (400mL can, "COOP 365 Økologi") was made by whipping a mixture of the milk, soy lecithin (emulsifier, "Condi Aps") and pure water (Milli-Q) to butter, after which the butter was cooled to harden. The butter was then split by mass into vials and had according amounts of

ground NaCl (VWR, Lot: 16F233134) added by mass, after which the samples were melted in luke warm water, vortexed for 30 seconds and cooled to solidification. The milk was noted to contain 71% organic coconut extract, water and Xanthan gum (E415).

The system based on coconut oil (Green Choice, "Organic Coconut Oil Neutral Taste) was made by melting the oil and transferring it to vials. Based on mass, aqueous solutions of NaCl were prepared and added to the vials. The samples were then vortexed for 30 seconds and cooled to solidification. The coconut oil was noted to contain 100% organic refined coconut oil.

All samples were stored at 5°C.

3.4 Matlab Dataanalysis

The following section will discuss the scripts created in Matlab that are used to determine the concentration of salt within waterdroplets in butter.

3.4.1 Calibration to Signals from Aqueous Solutions of Ions

The images of aqueous solutions of NaCl are chosen by the user, then imported into the working environment of Matlab. The images are sorted according to their filename, after which the script verifies that all imported images are pairs at the different wavenumbers ν_1 and ν_2 , that the pairs are the same size and that all images contain a file from each direction of detection. The file specifying the concentrations of salt in each sample is then imported.

Next, the script will calculate the mean intensity of each image, then calculate the mean intensity of the five retakes at each location within the sample. Based on this, the script will attempt to remove bad data-points. This is done as the laser - after tuning - is not always able to reach the intensity; hence clear outliers will be present in the data set. The script identifies an outlying data-point by calculating a linear fit for all data-points, after which it considers the data-point that is furthest away from the linear fit. If this data-point deviates from the linear fit by more than a chosen percentage, relative to the value of the linear fit at the specific concentration of salt, the data-point is discarded and the linear fits is calculated again. This process continues untill all data-points are within the allowed deviance. The allowed deviance is based on preliminary measurements, that are described in the results section.

Finally the script will calculate the mean and standard deviation of measurements at each concentration of salt and create a plot, based on the remaining data-points and the linear fit of these. This is done for each wavelength and for each direction of detection. The output of the script is the plots, the linear fits and a list of the images that were discarded due to unstable tuning.

When performing the calibration, it is expected that any determined relation between relative signal and concentration of NaCl is unique for that specific setup; a change of ions, detectors, detector bias, direction of detection and even relative laser intensities are expected to change the behavior of the system and measurements.

3.4.2 Determining Concentration of Ions in Butter

The images of butter from one sample are chosen by the user, after which they are imported into Matlab. The images are sorted according to their filenames and the script will attempt to verify that all images are pairs at different wavelengths, that the pairs are the same size and that all images contain a file from each direction of detection.

All images are then smoothened and the droplets of water, for now referred to as regions of interest (ROIs), are automatically detected using Otsu's method [26]. The ROIs are detected in the images acquired at the wavenumber that yields the most intense signal: ν_1 . The detected ROIs that are smaller than four pixels or larger than 20 % of the whole image are removed and the mean intensity of each ROI is calculated at both ν_1 and ν_2 . Then the relative intensity is calculated for each ROI by dividing the mean intensity at ν_2 by the mean intensity at ν_1 . The relative intensity of each ROI is used to determine the concentration of NaCl within each droplet of water. The script converts the area of each ROI from pixels to micrometers and outputs the following determined values to a *.txt*-file:

- weighted mean of salt concentration in droplets
- standard deviation of salt concentration in droplets
- mean of droplet areas
- standard deviation of droplet areas
- the sum of the droplet areas
- the sum of areas of images used for the dataanalysis
- the fraction of total droplet area per total area of images
- an estimation of the salt concentration of the whole sample

Finally the script plots the distribution of the concentration of salt and size of the droplets determined from each direction of detection.

Chapter 4

Results

The following chapter initially presents the results related to the development of the SRS-system, after which the results obtained during the calibration as well as the results obtained from the method for determining the concentration of salt in samples of butter are shown.

4.1 SRS Microscope

The results related to the creation of the SRS microscope, obtained during this project are described below.

4.1.1 Detector and Bias

The behavior of the detector under illumination with the 816.4nm laser light which will be used for the SRS-imaging, was investigated by viewing the signal from the detector using an oscilloscope. An image of the signal is shown in figure 4.1. To avoid interference from other sources than the laser, the detector was mounted inside a 10cm tube with a shutter closed as much as to only allow for the laserbeam to pass, while the room light was off.

Prior to the measurements, it was confirmed that the tube with the detector was aligned with the laser beam. This was done by viewing the signal from the detector using an oscilloscope and then moving the tube with the detector to maximize the amplitude of the signal. As the peak-to-peak value of the signal is maximized, the detector is aligned optimally for the close-to-normal angle of the light incident on the surface of the detector.

From figure 4.1 it can be seen how the detector is actually able to distinguish the 80MHz pulses of the 816.4nm laser at a bias of 20V - contrary to what would be expected from the rise/fall time of the detector. However, it should be noted, that the DC-offset in the signal (which is not shown directly in the image) is due to the rise/fall time of the detector. The rise/fall time is too long to allow the detector to reach 0V output between the pulses of laser light; hence the presence of the DC-offset in the signal.

Another important detail to notice from figure 4.1 is the displacement of the center of oscillation of the AC-signal, relative to the DC-signal. The DC-signal is indicated by the small arrow with a "1" furthest to the left in the image. The

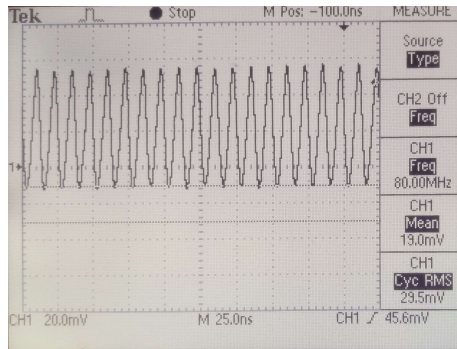


Figure 4.1: Image of the oscilloscope screen viewing the AC-signal from the detector being illuminated by 816.4nm 100mW laser power at a bias of 20V.

displacement is due to the trigger level (indicated by the small arrow on the right side of the signal), which has been set as far from the DC-signal as possible, to show a more clear signal. The displacement of the center of oscillation indicate that the signal is superimposed on a slower oscillation in the signal. This slower oscillation is shown in figure 4.2.

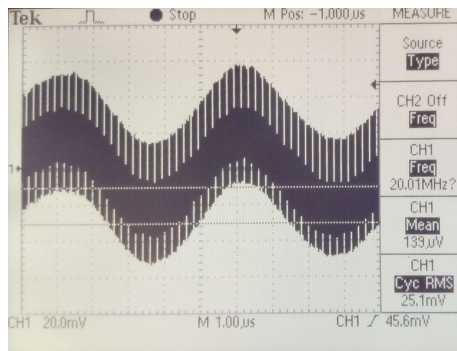


Figure 4.2: Image of the oscilloscope screen viewing the AC-signal from the detector being illuminated by 816.4nm 100mW laser power at a bias of 20V. N.B. the seemingly jagged signal is derived from the recording of the signal prior to decreasing the viewed timeframe; this is merely a display of the oscilloscope's finite memory and has no effect on the shape of the signal.

From figure 4.2 it can be seen that the 816.4nm pump laser changes intensity over a period of around $5.5\mu\text{s}$, which is equal to a frequency of approximately 182kHz. The fluctuation was observed to be linked to the laser light, as it was not observed when the laser shutter was closed. The change is considerably slower than the modulation used for the SRS-imaging and is therefore expected to be completely removed by the lock-in amplifier.

As the pump laser was experienced to change intensity over time, the Stokes laser was investigated as well. The signal from the detector being illuminated by the Stokes laser was also viewed using an oscilloscope. This is shown in figure 4.3.

From figure 4.3 it can be seen how the AC-component of the signal has a

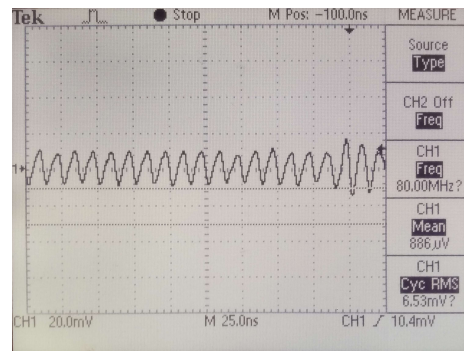


Figure 4.3: Image of the oscilloscope screen viewing the AC-signal from the detector being illuminated by 1064nm 100mW laser power at a bias of 20V.

center of oscillation that is around the DC-component. To the right in the image can be seen how the signal changes slightly. The slight change was investigated and found to have a period of about $5\mu\text{s}$. This slow change is not expected to affect the SRS-imaging, as it will be removed by the lock-in amplifier.

The signal from the detector was also observed to contain noise that is independent of the light incident on the detector. To investigate the noise and locate the source, the noise is viewed using an oscilloscope. This is shown in figure 4.4.

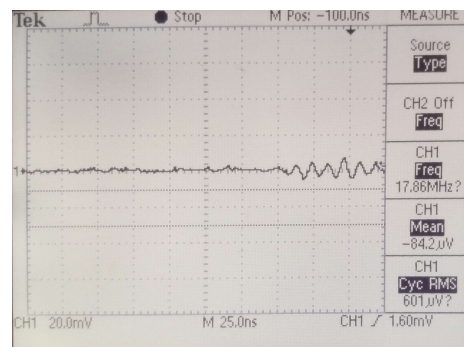


Figure 4.4: Image of the oscilloscope screen viewing the AC-signal from the detector not being illuminated by any light.

From figure 4.4 it can be seen how the noise is made up by pulses that appear to have a frequency very close to 10MHz. Therefore the lock-in amplifier will not be able to remove the noise, when creating images with the SRS-technique. The source of the noise was determined to be the microscope-table on which the detector was mounted. Furthermore, it was noted that the system was still affected by random noise, that was found to be picked up in the analog-to-digital (ADC) converter, which converts the analog signal from the lock-in amplifier to a digital version that the PC can interpret. The ADC is surrounded by cables and power supplies, which are all known to be sources of noise.

Furthermore the signal from the detector being illuminated by 1064nm laser light modulated at 10MHz was investigated. An image of the signal is shown in

figure 4.5.

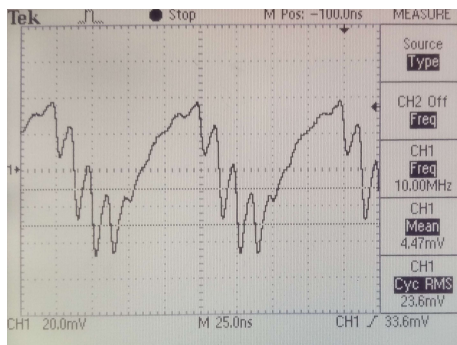


Figure 4.5: Image of the oscilloscope screen viewing the AC-signal from the detector being illuminated by 1064nm laser, modulated at 10MHz, at a power of 100mW and a bias of 20V.

From figure 4.5 can be seen how the modulation affects the signal from the detector. It is important to remember that the detector responds with a negative voltage that is proportional to the power of the incident light; hence the greater the illumination, the lower the position of the signal on the screen of the oscilloscope. This relates to the rise/fall time, as is seen in figure 4.5, the peaks are hardly recognizable when the modulation starts to reduce the power of the individual 80MHz pulses. On the contrary, the individual peaks are easily recognizable when the modulation allows for increasing power to reach the detector. This asymmetrical response is explained by the rise/fall time being slower than the repetition rate of the individual pulses of light; the power is decreased faster by the modulation, than what the detector is able to keep up with. This may be verified by increasing the bias voltage, which leads to an increased temporal resolution; hence the individual peaks will be more easily distinguishable when the laser power is decreasing.

The behavior of the detector was investigated by measuring the voltage output at different intensities of laser, incident on the surface of the detector. The result of the measured response to the varying power of the laser is shown in figure 4.6.

From figure 4.6 it can be seen how the detector works over a certain range of intensity of incident light: 0 – 250mW. After 250mW of laser power, the linear relationship between incident light and DC-output cease to be and at a laser power of 600mW or more, the detector is overloaded and its output falls to 0V. The AC-component can be interpreted as a measure of the detectors response to high-frequency fluctuations in the incident light. From figure 4.6 a maximum around 100 – 150mW can be seen, which indicate maximal sensitivity towards high-frequency fluctuations at the center of the working range of incident light. The broadness of the working range was determined at two different bias-voltages, the results are shown in figure 4.7.

From figure 4.7 it can be seen how a working range of 0 – 150mW can be achieved with at least 15V bias (as the measurement stabilizes after this bias), while a working range up to 450mW demands more than 30V bias. The AC-component of the 150mW measurement is seen to continually grow after 15V

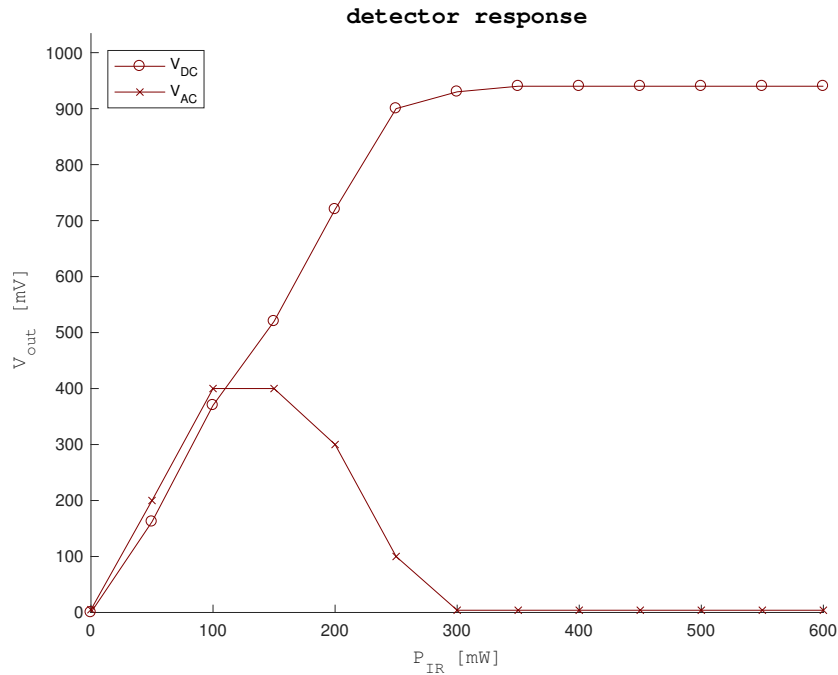


Figure 4.6: Measured response of detector at varying power of the 1064nm laser with a 20V bias. N.B. the AC-signal has been amplified 10 times.

bias; a higher bias allows for increased temporal resolution, as is expected from (3.2). The linear response between bias and output-voltage in the 150mW AC-component, indicate that the bias is sufficient for the detector to distinguish the high-frequency fluctuations at the given intensity; hence the onset of the linear response shows the minimal bias required for the detector to distinguish the high-frequency fluctuations in the incident light. Furthermore it can be seen that a greater incident power, demands a greater bias, for the detector to be able to follow the high-frequency fluctuations in the light. Finally it should be noted that the slight deviance between measured values of V_{out} at 450mW of laser power at a bias of 20V is due to the precision of the power supply for the bias, which was adjusted during measurements.

The responsivity of the detector was unfortunately not measured for a wavelength of 816.4nm, which on this system is equivalent to 2850cm^{-1} (lipid), as the laser malfunctioned during the measurements. The measurement was not attempted again, as the behavior of the detector is expected to be close to the same as for the 1064nm measurements. Finally the efficiency of the optical filter used to remove the modulated 1064nm laser during the SRS-imaging was investigated. No change in the output-voltage from the detector, under a bias of 20V, was observed, even at a maximal power of 600mW.

4.1.2 Reference Signal Amplifier

The reference frequency signal from the laser was initially observed as shown in figure 4.8 (left). The signal is seen to not reach the voltage levels required for

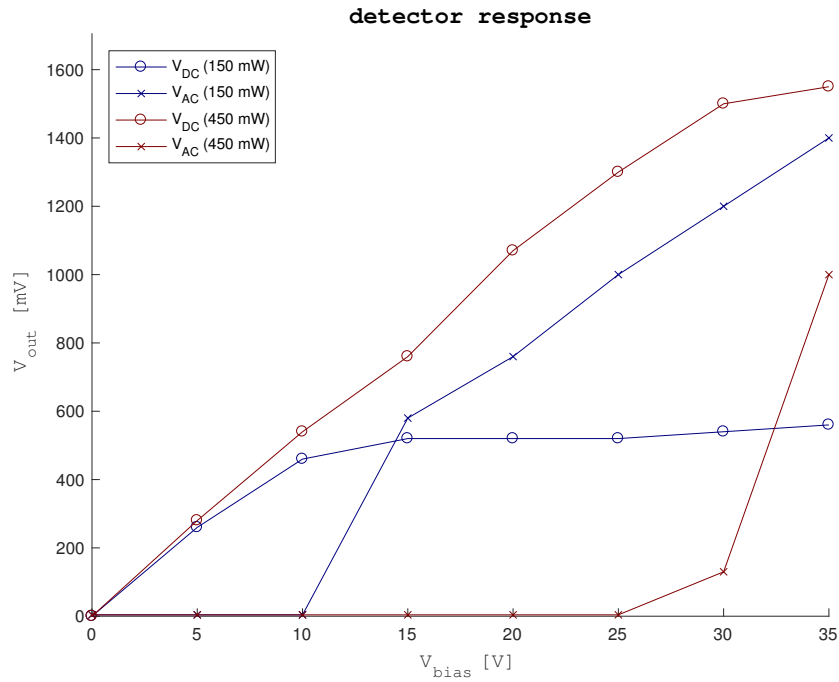


Figure 4.7: Measured response of detector at 150mW and 450mW 1064nm laser, at varying bias voltages. N.B. the AC-signals has been amplified 10 times.

the "high" bit (2 – 5V) of a TTL-signal; hence an amplifier was made for the signal. The amplified signal is shown in figure 4.8 (right).

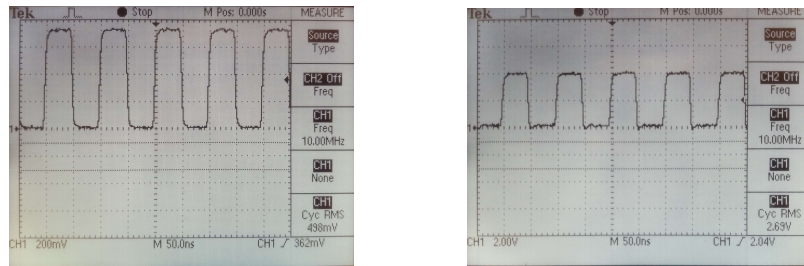


Figure 4.8: Left: reference signal from the laser before amplification. Right: reference signal from the laser after amplification.

From figure 4.8 (left) it can be seen how the peak voltage of the signal is 700 – 750mV. The amplified signal shown in figure 4.8 (right) is seen to have a peak voltage of 4V; hence the amplified signal is a valid TTL-signal. Upon providing this signal to the lock-in's reference port, the frequency can be seen to stabilize around 10MHz, while still fluctuating with ± 10 kHz. If the detector is connected to the lock-in and illuminated with modulated laser-light, the phase (and R -value) can be seen to stabilize, indicating that the lock-in is working as it is supposed to.

4.1.3 Lock-in Amplifier

The phase-independent amplitude R is the value that is of interest to create an image with the SRS-technique. This value can be read directly from the screen of the lock-in amplifier or from the related analog output-port on the back of the instrument. As an initial test of the lock-in amplifier's ability to sort out frequencies that are different than the reference, the phase-independent amplitude was measured for different settings of order of the roll-off filter, by setting the lock-in amplifier's internal clock to 10MHz and changing the frequency of a function generator connected to the lock-in's input port. The results are shown in 4.9.

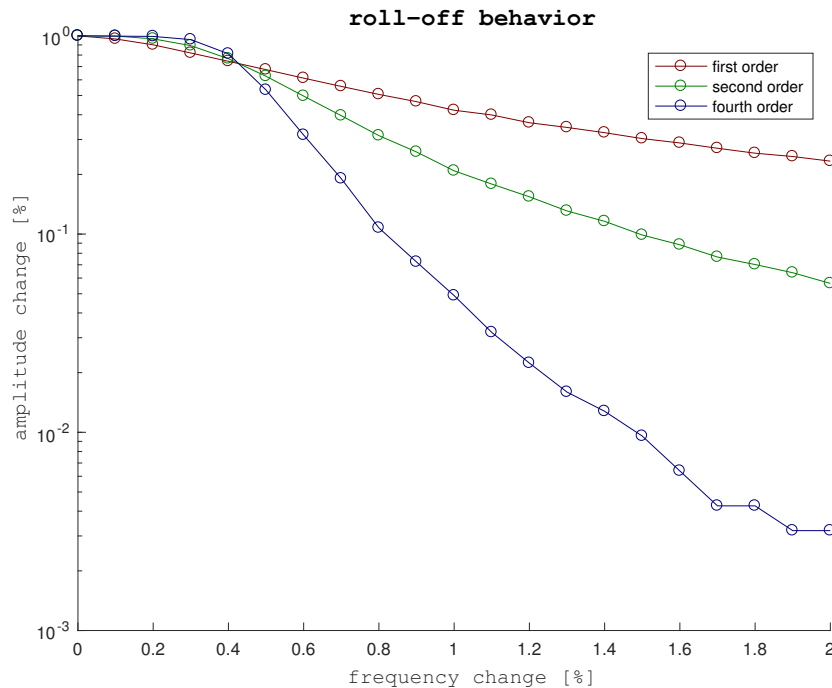


Figure 4.9: Measured behavior of amplitude of signal around 10MHz, at different settings of roll-off filter order.

The roll-off behavior was only measured for frequencies of 10MHz and higher, as the roll-off behavior is expected to be symmetrical around the reference frequency. From figure 4.9 it can be seen that the fourth-order filter is capable of rejecting 99% of a signal that is more than 1.5% different in frequency. The filters have therefore been shown to work as expected, though only on a small part of the full range of operation. For an investigation of the capability of the filters at their full range of operation, please refer to [23].

To confirm the lock-in amplifier's ability to detect the phase-difference and adjust to this automatically, the output of a function generator was split and provided to both the reference port and the input port of the lock-in amplifier, using different lengths of cable. The difference in cable-length produces a phase-difference between the signal received by the lock-in amplifier in its different ports. The lock-in proved to be able to detect the phase-difference

automatically by stabilizing the detected phase ($\pm 1^\circ$) as well as the R -value ($\pm 0.5\%$ of measured value).

When considering the integration time t , it is important to consider the modulation frequency of the laser. The smallest reasonable integration time has to be big enough for the lock-in amplifier to consider at least one full period of oscillation, to obtain correct results for the measurements. The smallest reasonable integration time for a frequency of 10MHz is calculated in (4.1).

$$t_{min} = \frac{2\pi}{10\text{MHz}} = 628\text{ns} \quad (4.1)$$

From (4.1) it can be seen that one period of oscillation at the reference frequency is 628ns long; hence the integration time t must be longer than this time, for the lock-in to calculate a correct result. In reality the integration time was set at $20\mu\text{s}$, which was observed to generate the smallest amount of noise, while generating an image that was as clear as it could be.

4.1.4 Imaging with SRS Microscope

Before trying to acquire any images, it was made sure that the two laser beams were perfectly aligned in the xy-plane. This was done by illuminating fluorescent beads by each laser separately and ensuring that the beads were positioned identically in the two images. After this, the available objectives were investigated to determine which one provided the best overlap in the z-direction. The objective with the best overlap was found to have a $0.3\mu\text{m}$ distance between the focal points of each beam. To test the effect of the lock-in amplifier, it was attempted to obtain images of the fluorescent beads, illuminated by the 1064nm laser, being either modulated at 10MHz or not modulated (80MHz). The images are shown in figure 4.10.

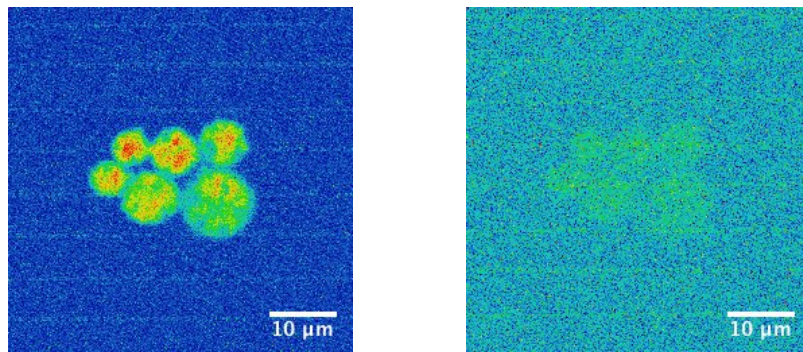


Figure 4.10: Images of fluorescent beads at 1064nm at $60\times$ magnification. Both images are obtained through the SRS microscope-system. Left: Image obtained using 10MHz modulated laser. Right: Image obtained using unmodulated 80MHz laser.

From figure 4.10 it can be seen that the SRS-system is capable of producing fluorescence images, though still affected by noise. The SRS-system proves capable of removing signals at a frequency different from 10MHz, which is seen by the clear difference between the two images. Both images are however affected

by noise (horizontal lines). Based on the dimension of the image: 256×256 pixels, the dwell-time set for each pixel: $64\mu\text{s}$ and the periods of noise per image: 8, the frequency of the noise can be approximated to 2Hz. This noise is mostly introduced to the image in the analog receiver, which explains why it is not removed by the lock-in amplifier. If the noise was introduced to the signal before the lock-in amplifier, the noise has to be carried by a 10MHz wave to pass.

The imaging capability of the system was investigated by using the already present CARS-capability of the microscope to obtain images using both CARS and SRS at the same location within the sample NS1. This is shown in figure 4.11.

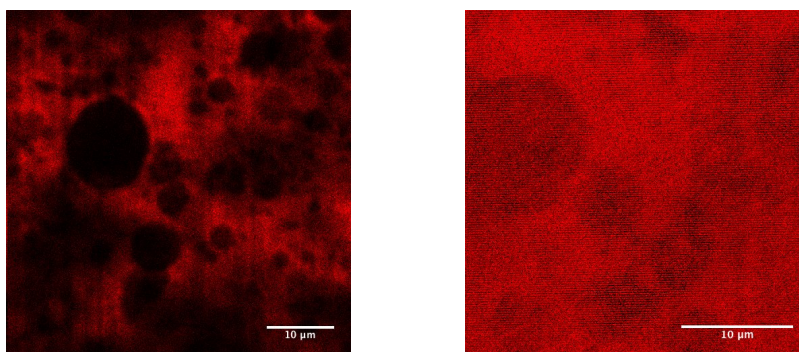


Figure 4.11: Images were acquired at the exact same place, both at 2850cm^{-1} (lipid), in the sample NS1 at a pump laser power of 450mW and a Stokes laser power of 600mW. Left: CARS-technique. Right: SRS-technique.

From figure 4.11 can be seen how the system is capable of producing images using the CARS-technique; hence the focus is properly positioned inside the sample for an image to be created. Though the CARS image is noisy, the CARS-effect is observed and therefore the SRS-effect is occurring as well. The SRS-image is expected to show the same structures - with less noise - but the structures cannot be directly related and the image is again affected by noise (horizontal lines and areas of pixels with inconsistent intensities).

It was attempted to image sample NS-1, at the two wavenumbers 3180cm^{-1} (water) and 2850cm^{-1} (lipid). The images are shown in figure 4.12.

As the two major constituents of butter are lipid and water, it is expected that the images in figure 4.12 are inverted relative to each other. The images barely show any structures and the structures that are observed in the two images are not comparable. This indicates that the system may have not been properly configured. The output range of the lock-in amplifier may have been set too low (from adjusting the output range while viewing a place within the sample, that does not give any signal at this wavenumber), to allow for a SRS-signal to be present without overloading the analog output of the lock-in amplifier.

Unfortunately it was not possible to make the SRS-microscope work properly, in time to obtain measurements using this technique. Therefore, it was decided to proceed with imaging the samples of butter by using the CARS-technique available at another microscope.

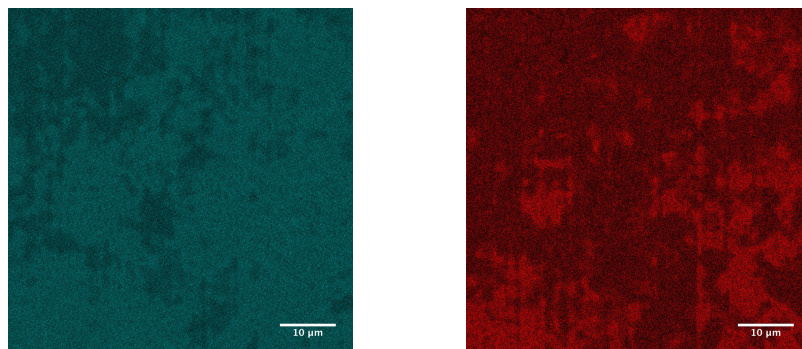


Figure 4.12: Images of the sample NS1 made using the SRS-technique at a $60\times$ magnification and 450mW pump laser power and 600mW Stokes laser power. Left: probing SRS-effect at 3180cm^{-1} (water). Right: probing SRS-effect at 2850cm^{-1} (lipid).

4.2 Calibration of Signal at Varying Concentrations of Salt

As an initial proof of method, the CARS spectra were obtained for increasing concentrations of NaCl in water. The spectra are shown in figure 4.13.

From figure 4.13 it can be seen how the intensity at the two marked wavenumbers change with the concentration of NaCl in aqueous solution, this is also shown in [21]. Based on the coordination of water that is described in the theory, the wavenumber 3180cm^{-1} may be assigned to the 4-coordinated water molecules and 3340cm^{-1} to the remaining lower-coordinated water molecules. The intensity of the signal at 3180cm^{-1} is observed to decrease with increasing concentrations of NaCl, while the intensity of the signal at 3340cm^{-1} is observed to increase. The relative intensity, observed for these wavenumbers, is used to infer the concentration of NaCl. By using the relative intensity, it is possible to obtain a measurement that is invariant to parameters that would otherwise affect the intensity of the signal. Images of varying aqueous solutions of NaCl were acquired using CARS at two different wavenumbers: 3180cm^{-1} and 3340cm^{-1} . Images of pure water are shown in figure 4.14.

The mean intensity of images as in figure 4.14 was observed to exhibit a trend but also deviate greatly from the trend. Therefore the variance between results was investigated in relation to changing parameters during the acquisition of images. The variance of results compared to the distance to the glass/water interface of the microscope slide is shown in figure 4.15. The variance is determined from five individual measurements for each direction of detection at 3180cm^{-1} .

From figure 4.15 it is seen how the variance drops as the measurement is done more than $10\mu\text{m}$ away from the glass/water interface. The increased variance experienced close to the interface may be due to the uncertainty regarding the thickness of the microscope slide, where water molecules close to the glass surface are expected to interact with the surface of the silicon-oxide glass material. This affects the coordination of the water molecules; hence the signal is expected to change in the presence of a glass-surface. Furthermore the variance

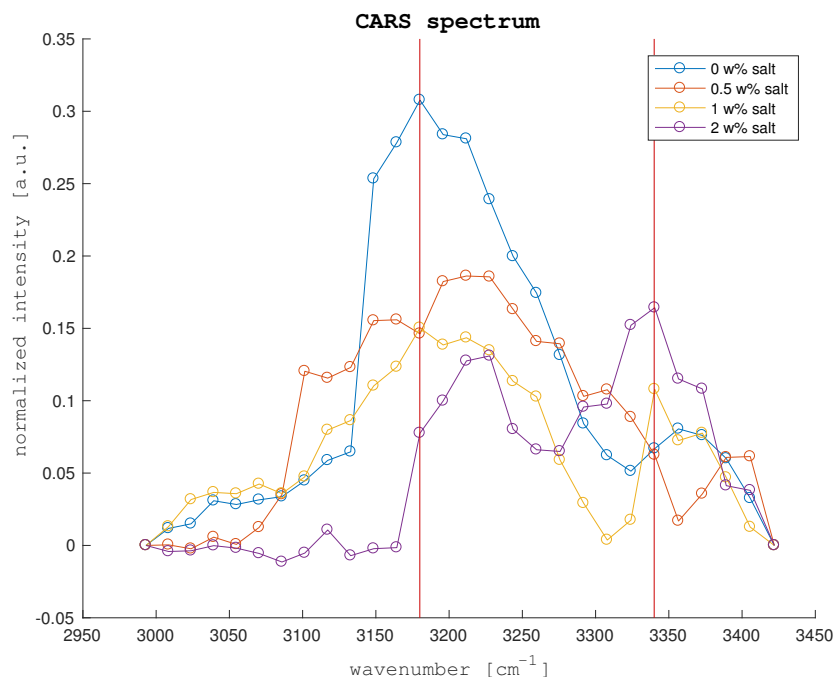


Figure 4.13: CARS spectra measured for four different concentrations of aqueous solutions of NaCl. The vertical red lines mark the wavenumbers 3180cm^{-1} and 3340cm^{-1} , which are later used to determine the concentration of NaCl. N.B. normalization is made by subtracting a linear interpolation, made between the endpoints of measurements, from the measured values.



Figure 4.14: Images of pure water, acquired using CARS. Left: probing 3180cm^{-1} . Right: probing 3340cm^{-1} .

was investigated as the focus was moved in the xy-plane, as well as for tuning between the wavenumbers 3180cm^{-1} and 3340cm^{-1} . The determined variances are shown in table 4.1.

From 4.1 it is clear that the tuning of the laser is the major contributor to the variance between measurements. This was realized to be due to the laser not reaching the set intensity - even though the program controlling the

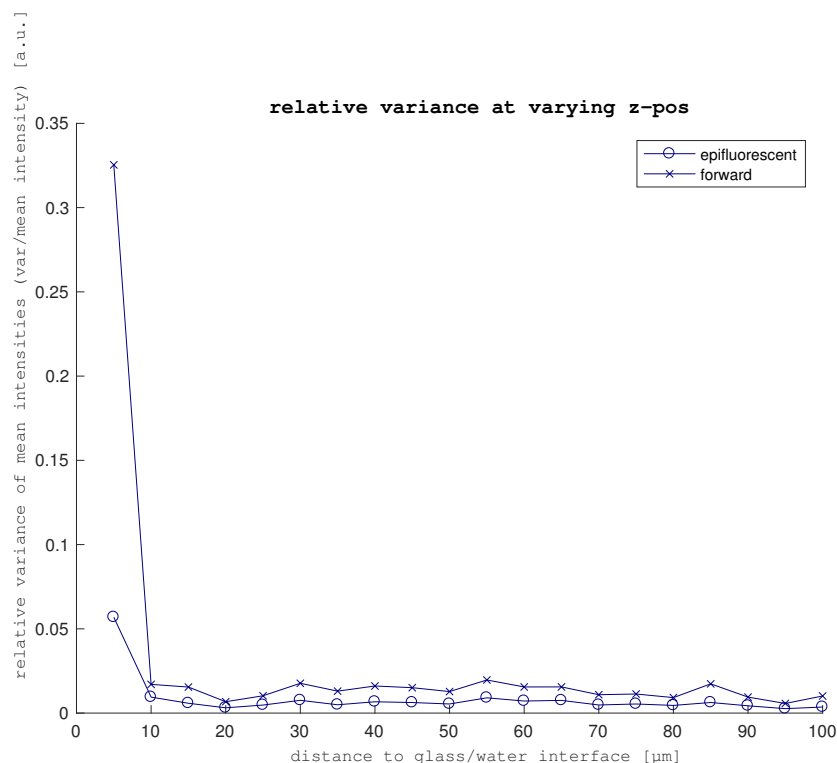


Figure 4.15: Determined variance of results, related to the distance to the glass/water interface at the microscope slide.

parameter	relative variance	
	forward	epifluorescent
z-pos	< 2.5%	< 1%
x/y-pos	< 10%	< 0.025%
tuning to 3180cm^{-1}	< 120%	< 10%
tuning to 3340cm^{-1}	< 170%	< 20%

Table 4.1: Variance-measurements on pure water. N.B. the determined values only apply when the distance to the glass/water interface is greater than $10\mu\text{m}$.

laser stated that it had finished tuning and reached the set intensity. Based on this realization, the jagged behavior of the spectra in figure 4.13 can be explained. Therefore it should be noted that some data-points deviate and that these measurements should only be considered in a qualitative way. The intensity was measured five times in a row, at each wavenumber, at five different locations in a sample (at a distance of $100\mu\text{m}$ from the glass/water interface) for eight different concentrations of NaCl in water. To elucidate the functioning of the sorting algorithm used for the salt calibration measurements, the results before and after sorting are shown for the epifluorescent direction of detection at 3180cm^{-1} in figure 4.16.

From figure 4.16 it can be seen how the sorting algorithm is capable of re-

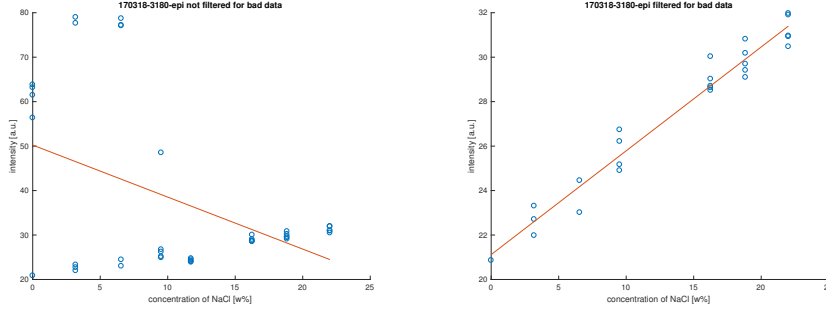


Figure 4.16: Epifluorescent-detected intensity-measurements at varying concentrations of NaCl in water, measured at 3180cm^{-1} . Left: all measured data-points, before removing bad data. Right: Data-points that are left after the sorting algorithm has worked on the data.

moving the clear outliers shown in the top left of the unsorted plot. Another part of the data that is removed, is the whole measurement at $12\text{w}\%$. The removal of all data-points may be justified by the possibility that the laser did not reach the set intensity for any of the measurements. This is, however, unlikely and should be investigated in the future. After the removal of outliers, the intensity is observed to exhibit a linear behavior in regard to the concentration of NaCl in solution. The results obtained from forward-detected images are shown in figure 4.17.

From figure 4.17 it is seen how the behavior of the intensity at the two wavenumbers appear to be linear and not changing at the same rate. The results obtained from the epifluorescence-detected images are shown in figure 4.18.

From figure 4.17 it is again seen how the behavior of the intensity at the two wavenumbers appear to be linear and not changing at the same rate. Furthermore it is seen that the change in the epifluorescent direction is more subtle, compared to the forward direction. This difference is merely an expression of the water's ability to scatter the light of the laser.

The linear fits of the change of the intensities are determined to be as shown in (4.2).

$$\begin{aligned}
 I_{for,3180} &= 1.279865 \cdot c_{NaCl} + 60.737177 \\
 I_{for,3340} &= 2.614713 \cdot c_{NaCl} + 38.543655 \\
 I_{epi,3180} &= 0.474638 \cdot c_{NaCl} + 20.976578 \\
 I_{epi,3340} &= 0.827782 \cdot c_{NaCl} + 17.951687
 \end{aligned} \tag{4.2}$$

From (4.2) it can be determined the relative intensity of the two wavenumbers, which in turn can be used to infer the concentration of NaCl in aqueous solution. This is shown in (4.3).

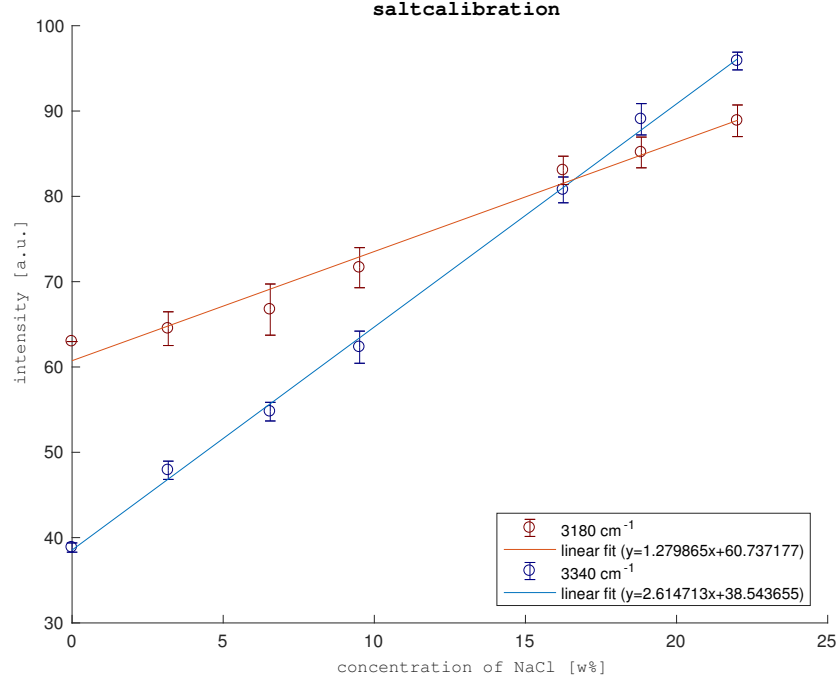


Figure 4.17: forward-detected aqueous NaCl solution calibration-curve. Standard deviation of measurements are shown as vertical lines around each measured point.

$$\begin{aligned}
 I_{rel,for} &= \frac{I_{for,3340}}{I_{for,3180}} \Leftrightarrow \frac{60.737177 \cdot I_{rel,for} - 38.543655}{2.614713 - 1.279865 \cdot I_{rel,for}} = c_{NaCl} \\
 I_{rel,epi} &= \frac{I_{epi,3340}}{I_{epi,3180}} \Leftrightarrow \frac{20.976578 \cdot I_{rel,epi} - 17.951687}{0.827782 - 0.474638 \cdot I_{rel,epi}} = c_{NaCl} \quad (4.3)
 \end{aligned}$$

The relations in (4.3) will be used by the Matlab-script to estimate the concentration of NaCl in the water droplets in the samples of butter.

4.3 Butter

Images acquired using the CARS-technique, feature a resolution in the z-direction that is adequate to create even 3-dimensional images. Such an image is shown in 4.19.

From figure 2.5 can be seen how droplets of different sizes are scattered throughout the lipid matrix. The laser used to create the image is incident from the behind lower right-side. It can be seen how the droplets of water act as lenses that diffract the laser. This effectively decreases the intensity of the laser on the opposite side of the droplet, creating the "shadow" effect. This is the reason behind the limited depth at which an image can be created in this type of sample.

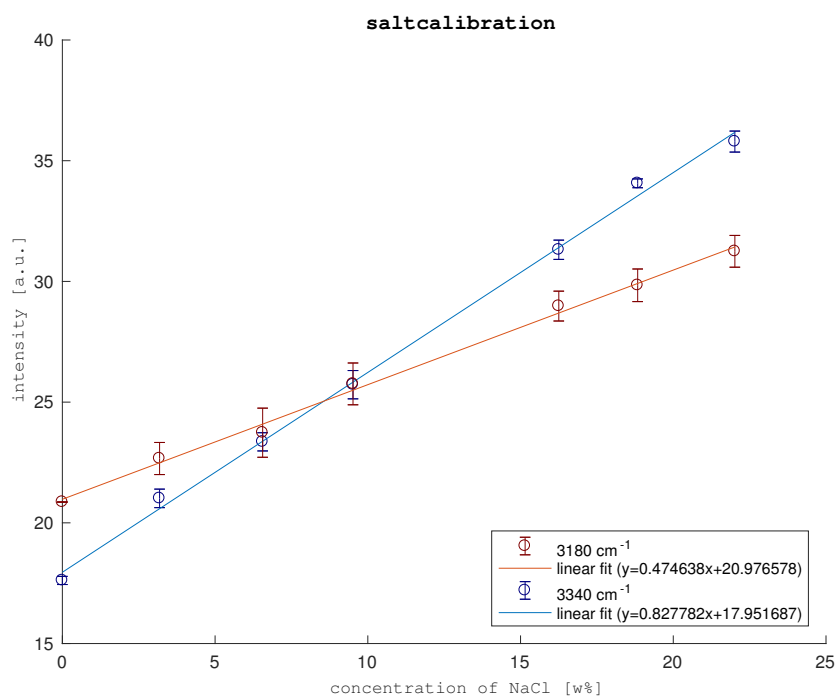


Figure 4.18: epifluorescence-detected aqueous NaCl solution calibration-curve. Standard deviation of measurements are shown as vertical lines around each measured point.

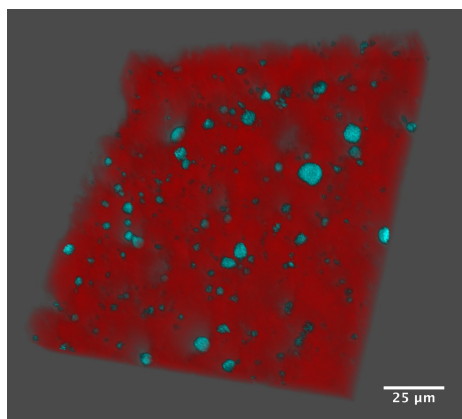


Figure 4.19: 3D image of butter. The image is a combination of two images: Blue: detected at 3185cm^{-1} (water). Red: detected at 2850cm^{-1} (lipid).

To be able to estimate the concentration of NaCl in the droplets of water within samples of butter, all images were acquired twice, one for each of the wavenumbers: 3180cm^{-1} and 3340cm^{-1} . As the laser was shown to sometimes fail in reaching the desired intensity after tuning, the images acquired - after a failed tuning - were useless for estimating the concentration of NaCl. To account

for the unstable tuning, all images were evaluated immediately after acquisition. If an image was observed to deviate in overall intensity, compared to the rest of the images from a sample, the tuning process would be repeated and another image was acquired. This was done as it was not possible, due to the complexity of the images, to create a dataanalysis-script in Matlab within reasonable time, that was able to sort between correct and incorrect measurements. Images of the sample NS-2, acquired at the two different wavenumbers are shown in 4.20.

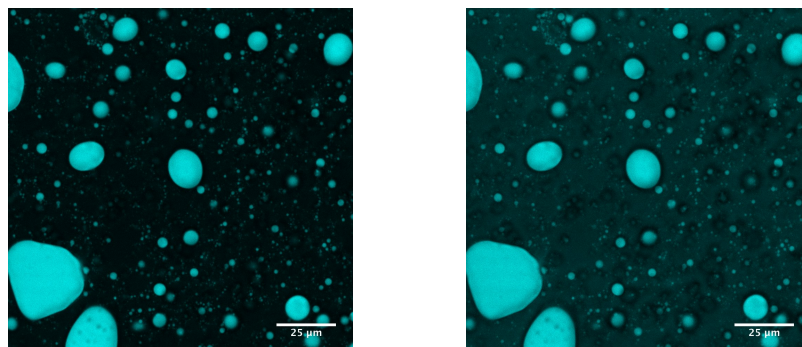


Figure 4.20: Epifluorescent-detected images of the sample NS-2. Left: acquired at 3180cm^{-1} . Right: acquired at 3340cm^{-1} .

From figure 4.20 it can be seen that images acquired at 3180cm^{-1} have a better contrast than the images acquired at 3340cm^{-1} . Furthermore, the epifluorescent-detected images are noted to have a slightly better contrast, compared to the forward-detected images. This is due to the fact that the images are acquired at a relatively small depth inside the sample, as the laser else becomes too scattered and diffuse to reach intensities, inside the focal volume, that are able to generate a CARS signal. The epifluorescent-detected images are made from backscattered light, which travels a shorter total distance through the sample, compared to the forward-detected images, which are made from light that has passed through the whole sample before being detected. Finally it should be noted that the dark spots inside the water droplet in the lower left corner of the images in figure 4.20 are shadows caused by smaller droplets, that are positioned closer to the light-source, than the large droplet. The shadow-effect is due to the droplet scattering the laser; hence the laser becomes too diffuse to generate a CARS signal.

While analyzing the data, the Matlab-script attempts to recognize the droplets. To verify that this is done properly, the script can be set to display an image from the analyzed set, overlaid with the borders of the detected droplets. An image of this is shown in figure 4.21.

From figure 4.21 it can be seen how the script is able to recognize the droplets in the image. The script outputs a plot showing the respective concentration of NaCl in relation to the area of each of the detected droplets, where the concentration is calculated from the relative intensities by using the relations determined in (4.2). This plot is shown for the forward-detected images of sample NS-1 in figure 4.22.

From figure 4.22 it can be seen how the distribution of the measurements are split into two. This is due to the laser not completely reaching the desired

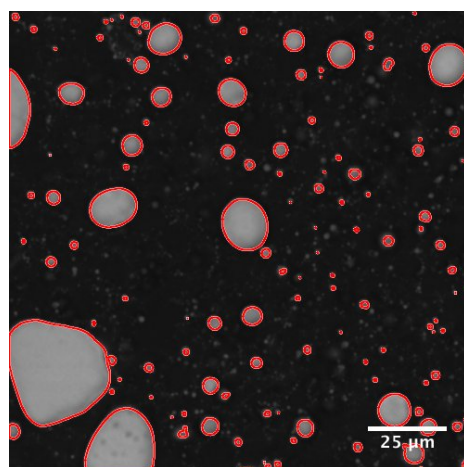


Figure 4.21: Epifluorescent-detected image of the sample NS-2, acquired at 3180cm^{-1} . The borders of the droplets that have been detected by the script are shown with red.

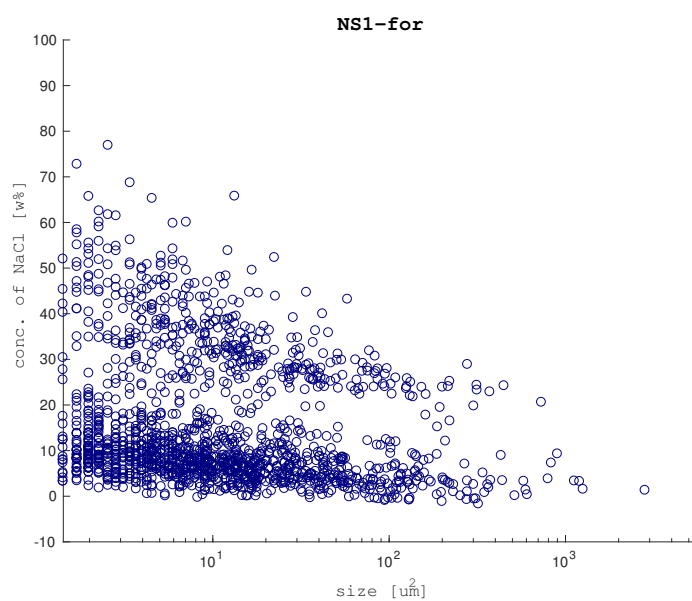


Figure 4.22: Plot of unsorted results from forward-detected images of sample NS-1.

intensity, yet the intensity was close enough for the first evaluation to not notice that the image was bad. All following results have been sorted manually for images that produce outlying measurements by first analyzing all images one pair at a time and then repeating analysis for all images together, omitting images that result in outlying measurements. The plots made from the epifluorescent-images are shown in appendix 7.1. These plots indicate the same trends as the forward-detected image-results, though an offset appears to be present for most measurements, which shifts the results towards lower concentrations of NaCl.

The sorted distribution of concentrations of NaCl and size of the droplets in the forward-detected images of sample NS-1, is shown in figure 4.23.

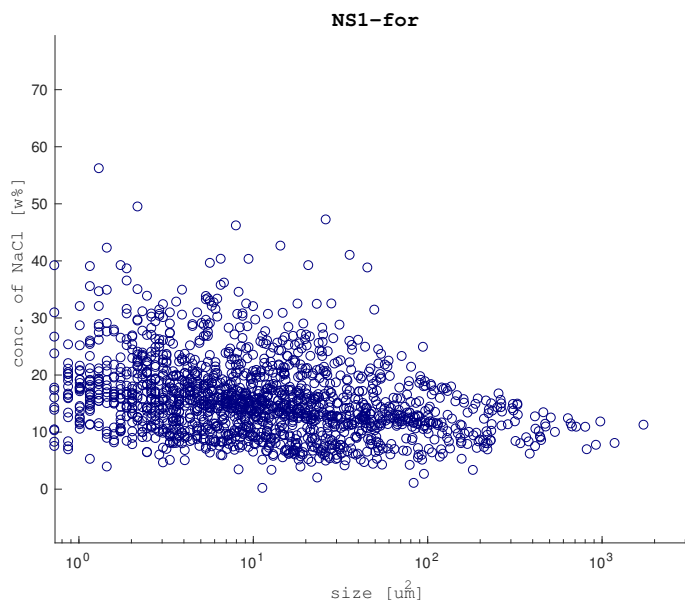


Figure 4.23: Plot of results from forward-detected images of sample NS-1.

results	forward	epifluorescent
$\bar{x}(c_{droplets})[w\%]$	12	4.8
$\sigma(c_{droplets})[w\%]$	4.8	6.1
$\mu(A_{droplets})[\mu m^2]$	36	36
$\sigma(A_{droplets})[\mu m^2]$	97	96
$x_{droplets/sample}$	0.081	0.082
$c_{sample}[w\%]$	1.1	0.43

Table 4.2: The weighted mean \bar{x} and standard deviation σ has been calculated for the salt concentration determined in the droplets. Furthermore the mean μ and the standard deviation has been determined for the areas of the droplets. Finally the total droplet area per image area-fraction x and the estimated salt concentration of the sample c_{sample} is shown. All values are related to sample NS-1.

From figure 4.23 it can be seen how most data-points are physically possible. No droplets are estimated to have a concentration of NaCl that is less than 0w% salt. A weak tendency towards smaller droplets containing slightly higher concentrations of salt, is observed. The results calculated for sample NS-1 are shown in table 4.2.

The distribution of the concentration of salt and size of the droplets in the forward-detected images from sample NS-2 are shown in figure 4.24.

From figure 4.24 it can be seen how a few of the data-points are greater than what is physically possible. Two droplets are estimated to have a concentration of less than 0w% and the majority of the estimated concentrations are

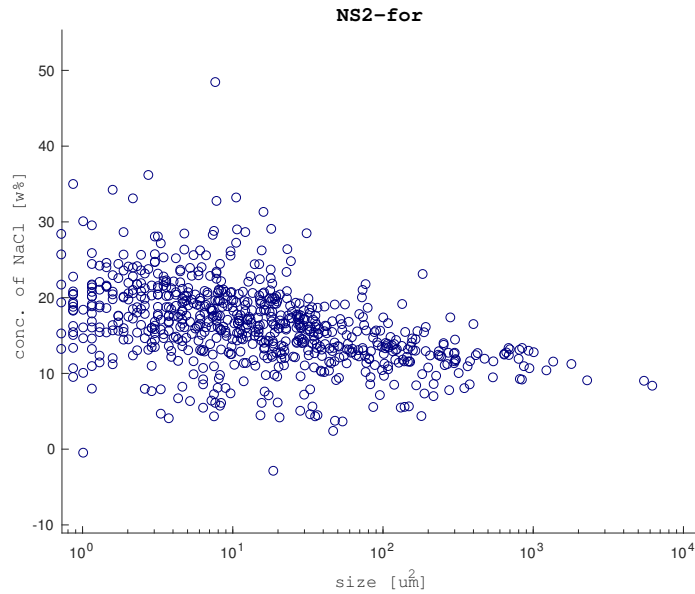


Figure 4.24: Plot of results from forward-detected images of sample NS-2.

results	forward	epifluorescent
$\bar{x}(C_{droplets})[\text{w}\%]$	12	5.1
$\sigma(C_{droplets})[\text{w}\%]$	3.3	4.1
$\mu(A_{droplets})[\mu\text{m}^2]$	80	79
$\sigma(A_{droplets})[\mu\text{m}^2]$	350	350
$x_{droplets/sample}$	0.082	0.084
$c_{sample}[\text{w}\%]$	1.1	0.47

Table 4.3: The weighted mean \bar{x} and standard deviation σ has been calculated for the salt concentration determined in the droplets. Furthermore the mean μ and the standard deviation has been determined for the areas of the droplets. Finally the total droplet area per image area-fraction x and the estimated salt concentration of the sample c_{sample} is shown. All values are related to sample NS-2.

observed to cluster at concentrations of around 17w% and show a slightly more pronounced tendency towards higher concentrations of salt in smaller droplets, compared to NS-1. The results calculated for sample NS-2 are shown in table 4.3.

The distribution of the concentration of salt and size of the droplets in the forward-detected images from sample NS-3 are shown in figure 4.25.

From figure 4.25 it can be seen how the majority of the droplets are estimated to have a concentration of salt around 10w%. Only one of the estimated concentrations are greater than what is physically possible and few are estimated below 0w%. This sample is seen to show a weak tendency towards lower concentrations of salt in smaller droplets, which is opposite of what is observed for samples NS-1 and NS-2. The results calculated for sample NS-3 are shown in table 4.4.

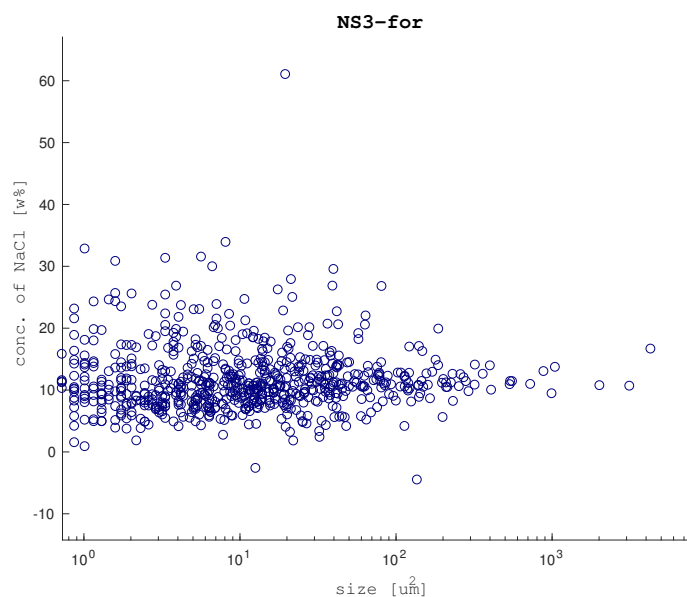


Figure 4.25: Plot of results from forward-detected images of sample NS-3.

results	forward	epifluorescent
$\bar{x}(c_{droplets})[w\%]$	12	5.1
$\sigma(c_{droplets})[w\%]$	3.7	4.4
$\mu(A_{droplets})[\mu m^2]$	49	48
$\sigma(A_{droplets})[\mu m^2]$	230	230
$x_{droplets/sample}$	0.081	0.084
$c_{sample}[w\%]$	1.1	0.47

Table 4.4: The weighted mean \bar{x} and standard deviation σ has been calculated for the salt concentration determined in the droplets. Furthermore the mean μ and the standard deviation has been determined for the areas of the droplets. Finally the total droplet area per image area-fraction x and the estimated salt concentration of the sample c_{sample} is shown. All values are related to sample NS-3.

The distribution of the concentration of salt and size of the droplets in the forward-detected images from sample NS-4 are shown in figure 4.26.

From figure 4.26 it can be seen how the data-points cluster around a concentration of 15 – 20w% salt. around twenty-five droplets are estimated at a physically impossible concentration. This sample exhibits a more uniform distribution of concentration of salt in relation to size of the droplet, compared to other samples, yet some data-points are observed to cluster at a lower concentration of salt. The results calculated for sample NS-4 are shown in table 4.5.

The distribution of the concentration of salt and size of the droplets in the forward-detected images from sample NS-5 are shown in figure 4.27.

From figure 4.27 it should be noted that around half of the estimated concentrations are physically impossible and data-points cluster at above 20w%

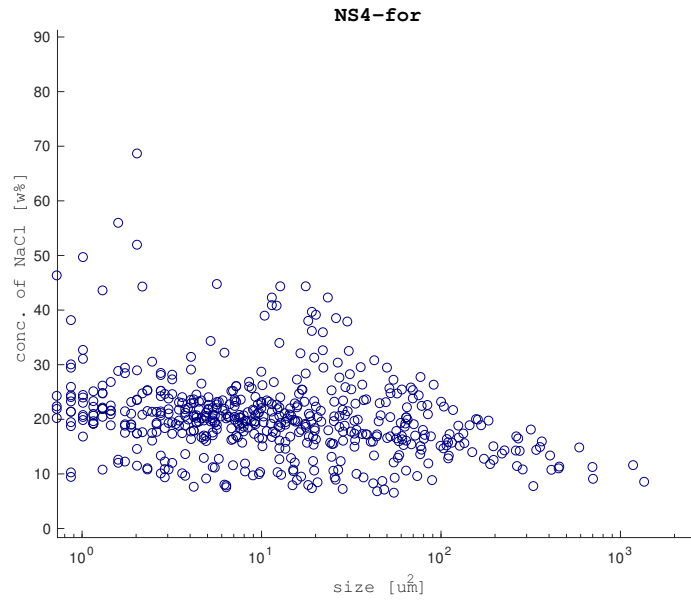


Figure 4.26: Plot of results from forward-detected images of sample NS-4 (organic).

results	forward	epifluorescent
$\bar{x}(C_{droplets})[\text{w}\%]$	15	9.6
$\sigma(C_{droplets})[\text{w}\%]$	5.8	8.1
$\mu(A_{droplets})[\mu\text{m}^2]$	41	41
$\sigma(A_{droplets})[\mu\text{m}^2]$	110	110
$x_{droplets/sample}$	0.077	0.078
$c_{sample}[\text{w}\%]$	1.3	0.82

Table 4.5: The weighted mean \bar{x} and standard deviation σ has been calculated for the salt concentration determined in the droplets. Furthermore the mean μ and the standard deviation has been determined for the areas of the droplets. Finally the total droplet area per image area-fraction x and the estimated salt concentration of the sample c_{sample} is shown. All values are related to sample NS-4 (organic).

salt. The results indicate a tendency towards higher concentrations of salt in smaller droplets, yet more proper images of this sample are needed to conclude anything. It should be noted that the size of the droplets in this sample are generally one half to a whole order of magnitude smaller, compared to other samples. It should be noted that the results shown in 4.27 are only based on one image-pair, as all other images yielded results that were physically impossible and meaningless. The results calculated for sample NS-5 are shown in table 4.6.

The distribution of the concentration of salt and size of the droplets in the forward-detected images from sample US are shown in figure 4.28.

From figure 4.28 it can be seen that many droplets are estimated to have a concentration of NaCl that is below 0w%, which is not physically possible.

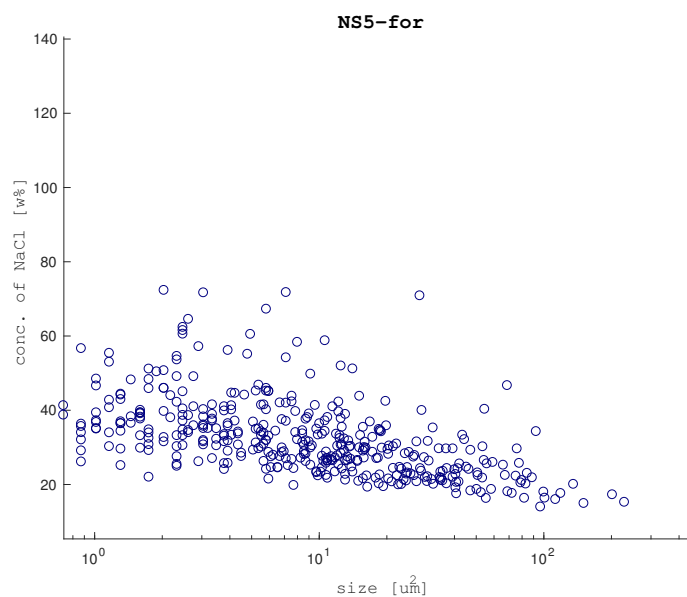


Figure 4.27: Plot of results from forward-detected images of sample NS-5 (25% vegetable oil).

results	forward	epifluorescent
$\bar{x}(c_{droplets})[w\%]$	26	19
$\sigma(c_{droplets})[w\%]$	8.9	13
$\mu(A_{droplets})[\mu m^2]$	18	18
$\sigma(A_{droplets})[\mu m^2]$	26	27
$x_{droplets/sample}$	0.050	0.052
$c_{sample}[w\%]$	1.4	1.1

Table 4.6: The weighted mean \bar{x} and standard deviation σ has been calculated for the salt concentration determined in the droplets. Furthermore the mean μ and the standard deviation has been determined for the areas of the droplets. Finally the total droplet area per image area-fraction x and the estimated salt concentration of the sample c_{sample} is shown. All values are related to sample NS-5 (25% vegetable oil).

However, the concentration of salt is derived from a relative intensity that is calculated from measurements that may fluctuate; hence some estimated concentrations of NaCl may be estimated below 0w%, while the mean of the measurements remains physically possible. The clustering of the data-points indicate a generally lower concentration of salt, compared to other samples. A tendency towards slightly higher concentration of salt in smaller droplets is observed. The distribution in the concentration of NaCl in droplets is more narrow, compared to other samples. The results calculated for sample US are shown in table 4.7.

The distribution of the concentration of salt and size of the droplets in the forward-detected images from sample HS are shown in figure 4.29.

From figure 4.29 it can be observed how the results indicate a very broad

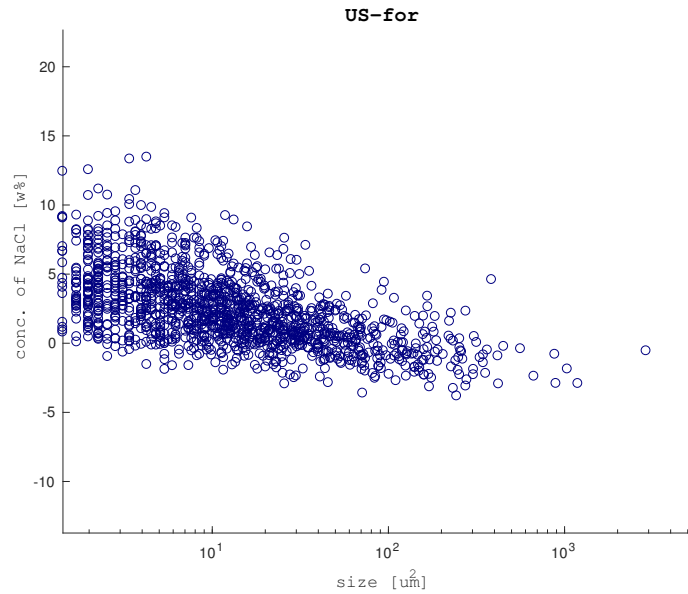


Figure 4.28: Plot of results from forward-detected images of sample US.

results	forward	epifluorescent
$\bar{x}(C_{droplets})[w\%]$	0.11	-8.4
$\sigma(C_{droplets})[w\%]$	2.1	2.3
$\mu(A_{droplets})[\mu m^2]$	35	36
$\sigma(A_{droplets})[\mu m^2]$	110	110
$x_{droplets/sample}$	0.042	0.042
$c_{sample}[w\%]$	0.01	-0.38

Table 4.7: The weighted mean \bar{x} and standard deviation σ has been calculated for the salt concentration determined in the droplets. Furthermore the mean μ and the standard deviation has been determined for the areas of the droplets. Finally the total droplet area per image area-fraction x and the estimated salt concentration of the sample c_{sample} is shown. All values are related to sample US.

distribution in concentrations of NaCl. The results indicate a clear tendency towards higher concentrations of salt in smaller droplets. It should be noted that the size of the droplets in this sample are generally one half to a whole order of magnitude smaller, compared to other samples. It should be noted that the results shown in 4.29 are based on one image-pair only. The results calculated for sample HS are shown in table 4.8.

At last it was attempted to acquire images of the two different well defined model butter-systems. An image of the sample based on coconut milk is shown in figure 4.30.

From figure 4.30 it can be seen that the sample resembles mayonnaise and not butter, as the lipid is organized in droplets with minute amounts of water in between. The sample is therefore not of any interest to study in this project. It is noted that the areas with relatively higher intensity in the image are due to

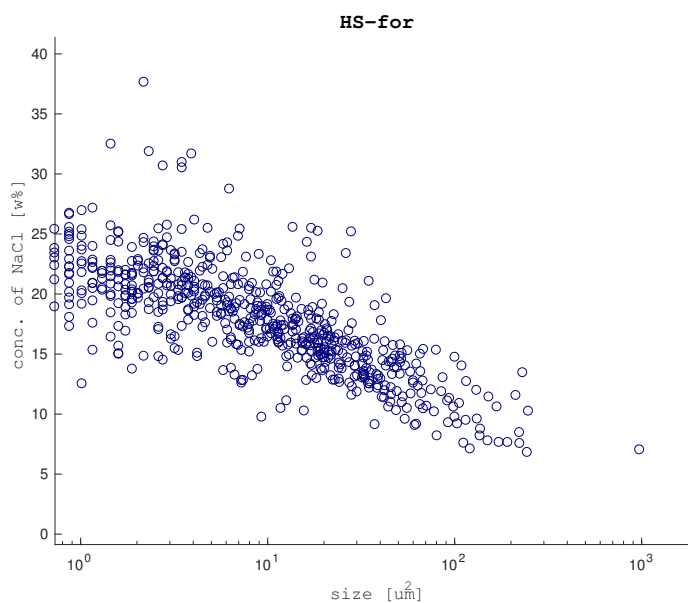


Figure 4.29: Plot of results from forward-detected images of sample HS.

results	forward	epifluorescent
$\bar{x}(c_{droplets})[w\%]$	13	8.4
$\sigma(c_{droplets})[w\%]$	4.2	6.3
$\mu(A_{droplets})[\mu m^2]$	22	21
$\sigma(A_{droplets})[\mu m^2]$	51	51
$x_{droplets/sample}$	0.097	0.104
$c_{sample}[w\%]$	1.4	1.0

Table 4.8: The weighted mean \bar{x} and standard deviation σ has been calculated for the salt concentration determined in the droplets. Furthermore the mean μ and the standard deviation has been determined for the areas of the droplets. Finally the total droplet area per image area-fraction x and the estimated salt concentration of the sample c_{sample} is shown. All values are related to sample HS.

larger droplets that are between the imaged plane in the sample and the laser source. The larger droplets scatter the laser less than the many small droplets; hence this sample is observed to produce a larger signal behind large droplets - which is the opposite of what is observed for the samples of butter!

When attempting to acquire images of the sample based on coconut oil, it was experienced to melt faster than an image could be obtained. It was not possible to find a solution that kept the samples properly cooled before the end of the project.

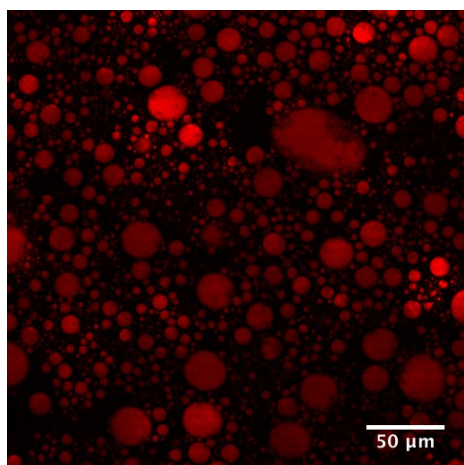


Figure 4.30: Forward-detected image of the butter-system made from coconut butter, containing 0w% salt. Imaged at wavenumber 2850cm^{-1} (lipid).

Chapter 5

Discussion

The discussion has been split up to reflect the major subjects covered through this project. The following sections will discuss the implications of the results obtained while characterizing the SRS-microscope, the dataanalysis-method as well as the calibration hereof and finally the results from the samples of butter.

5.1 SRS Microscope

Although a thorough characterization of the SRS-microscope was made, it was not possible to make the SRS-microscope capable of acquiring images of high quality. The investigation of the functioning of the SRS-microscope made it clear that by isolating the detector from the microscope and table, the noise observed in figure 4.4 was avoided. It was, however, noted that noise was picked up in the ADC that is connected to the PC.

By increasing amplification of the output from the lock-in amplifier, the effect of the noise may be reduced. On the other hand, a too small output range (from large amplification of output signal) will result in decreased contrast. This may be the reason for the lack of structures in the images in figure 4.12; as soon as even a small SRS-signal is present, the output signal overloads, resulting in a close to binary image.

Another issue that likely affects the images in figure 4.12 is the intensity of the pump laser being set too high. It was not possible to measure the intensity of light incident on the detector after passage through a sample, yet it can be estimated to be much too great, as the images were created at a pump laser power of 450mW, while the detector had a bias of 20V. It has been shown that the AC-signal from the detector - which is equivalent to the 10MHz signal that need to be measured to create an image with the SRS-technique - decreases when the incident laser power becomes too great and the detector is saturated. At a bias of 20V the incident laser power that yielded the greatest AC-response from the detector was determined to be 100 – 150mW, as shown in figure 4.6. It is indicated that the laser intensity needed for SRS is only around 10mW [27], which is considerably less than what has been used for the images in this project.

Of course the bias can be increased to broaden the optimal range of incident power, but at 450mW it was observed that the bias had to be greater than

25V for the AC-response of the detector to be measurable. The bias is only rated for a maximum of 25V; hence this is not a viable long-term solution. It was observed from figure 4.7 that an increase in bias led to an increase in AC-response (at 150mW) from the detector; hence the bias should be set as high as possible to increase the amplitude of the possible SRS-signal that the lock-in amplifier perceives from the detector. This is also in accordance with what is expected from the theory - increasing bias increases temporal resolution.

Furthermore, it was shown that it is possible to create a low quality CARS-image, while the quality of the SRS-image created at the same location within the sample was so low that the images could not be compared. The low quality of the SRS-image is implied from the low quality of the CARS-image; hence if the CARS-system is fixed, the SRS-system may produce high quality images as well. The low quality of the CARS-image is likely due to the fact that the laser beams were shown to not be properly overlapping in the z-direction. It was, however, possible to create a fluorescence-image using only one of the beams, which proves that the lock-in amplifier functions as intended.

5.2 Dataanalysis and Calibration

It may be interesting to see the CARS-spectra, as shown in figure 4.13, measured for a higher concentrations of NaCl in water (2 – 35w%). Furthermore the measured spectra may be repeated with greater resolution, to not only confirm the relative size and positions of the peaks, but also to try and determine if the wavenumbers that are probed may be adjusted to improve precision of the results - other wavenumbers than what are used in this project have been suggested in [9]. The peaks observed in the CARS-spectra shown in figure 4.13 were positioned relative to each other as described by [7, 8, 21], while the absolute positions of the major peaks were observed to coincide with what was described in [7, 8, 21].

Furthermore, it was shown how the laser is sometimes unable to reach the desired intensity after tuning. This makes it very laborious to obtain useful measurements, as the data analysis demands images at two different wavenumbers; hence all measurements have to be performed enough times to have statistical evidence to distinguish between useful measurements and incorrect tuning.

For the calibration of the dataanalysis, it is of course useful to do more measurements and increase evidence for the determined linear fits. As seen in figure 4.16, all measurements made at 12w% were removed by the sorting algorithm. This may be due to many consecutive bad tunings of the laser, but the possibility of a slight nonlinear behavior cannot be excluded yet. The CARS-signals of water at the two wavenumbers 3180cm^{-1} and 3340cm^{-1} were observed to exhibit a linear relation between intensity of signal and concentration of NaCl in the water. The signal at 3340cm^{-1} was observed to increase at a greater rate than the signal at 3180cm^{-1} with increasing concentrations of NaCl, which coincide with what was observed by Durickovic [21].

Regarding the detection of droplets, the borders are detected only in the 3180cm^{-1} -images, which is done to conserve time when analyzing images. The detected borders from the 3180cm^{-1} -images are used as basis when determining the mean intensity of the droplets in the 3340cm^{-1} -images as well. This method is only valid as long as the sample is not melting or moving while the

laser is tuning. It was considered to make the script detect droplets in images at both wavenumbers, though it was concluded to be too time consuming (within this project) to make sure that the script compares equivalent droplets in images at different wavenumbers. Furthermore measurements obtained from very small droplets are more easily affected by drift while the laser is tuning; the whole droplet may have moved completely out of focus between images at different wavenumbers. This problem was avoided by discarding measurements for droplets that are smaller than four pixels (compares to approximately $0.08\mu\text{m}^2$). For future uses, it may be considered to increase this limit, to obtain results that are less likely to be affected by drift and melting, though this ought not be a problem, when the protocol is followed.

5.3 Butter

As the epifluorescence-detected images were all affected by an offset in salt concentration, only the forward-detected images are discussed. The results based on the epifluorescence-detected images are, however, observed to display the same trends as results based on forward-detected images. An overview of the determined mean and standard deviation, as well as the droplet area per image area-fraction is shown in table 5.1.

sample	$\mu(A_{droplets})[\mu\text{m}^2]$	$\sigma(A_{droplets})[\mu\text{m}^2]$	$x_{droplet/sample}$	comment
NS-1	36	97	0.081	
NS-2	80	350	0.082	
NS-3	49	230	0.081	
NS-4	41	110	0.077	organic
NS-5	18	26	0.050	25% vegetable oil
US	35	110	0.042	
HS	22	51	0.097	

Table 5.1: Table listing mean μ , standard deviance σ and the fraction of droplets per area of sample x for all samples.

From table 5.1 can be seen how samples NS-1 to NS-4 all show similar values of droplet area per sample-fraction. The smaller fraction observed for sample NS-5 may indicate that the sample was prepared in the same way as the samples NS-1 to NS-4 and had the vegetable oil added in then end. Regarding the smaller fraction observed for sample US, an explanation for this may be that the salt-slurry never was added after the butter was produced; hence no more water was introduced to the butter. Furthermore the greater fraction observed for sample HS may be due to a greater amount of added salt-slurry.

From table 5.1 a trend is observed: the larger the mean droplet area, the larger the standard deviation. It is expected that a more thorough stirring, when adding salt-slurry to the butter, results in a decrease in the mean size of droplets of water. The sample HS exhibits smaller mean droplet area and standard deviation, indicating that this sample has been stirred for longer time; the higher concentration of salt may have been achieved by continually adding more salt-slurry. It should be noted for the HS sample, that whole flakes of salt crystals were present in the lipid matrix. The presence of whole flakes, that

have not been destroyed by the stirring of the sample, indicate that the salt flakes may have been added at the last stage of production.

In table 5.2 are shown all estimated concentrations of salt for the forward-detected images.

sample	$\bar{x}(c_{droplets})[\text{w}\%]$	$\sigma(c_{droplets})[\text{w}\%]$	comment
NS-1	12	4.8	
NS-2	12	3.3	
NS-3	12	3.7	
NS-4	15	5.8	organic
NS-5	26	8.9	25% vegetable oil
US	0.11	2.1	
HS	13	4.2	

Table 5.2: Table listing weighted mean \bar{x} and standard deviation σ of determined concentrations of salt within droplets for all samples.

From table 5.2 can be seen how the lower concentration of salt in sample US results in a lower weighted mean of the estimated concentration of salt within the droplets. The NS-5 sample is observed to have a much larger weighted mean concentration of salt. Upon further investigation of the images, it was clear that all images of sample NS-5 acquired at 3180cm^{-1} were dark, compared to other samples. The lower intensity is likely due to the laser not reaching the desired intensity after tuning and the imaging of this sample should be repeated. This is supported by the relatively large standard deviation, indicating that this result was not determined with the same precision as the other measurements.

In table 5.3 are listed all determined concentrations of salt for the whole sample.

sample	$c_{salt}[\text{w}\%]$	$c_{sample}[\text{w}\%]$	comment
NS-1	1.2	1.1	
NS-2	1.2	1.1	
NS-3	1.2	1.1	
NS-4	1.2	1.3	organic
NS-5	1.2	1.4	25% vegetable oil
US	0	0.01	
HS	1.9	1.4	

Table 5.3: Table listing determined concentrations of salt for all samples.

The values seen in table 5.3 show a clear trend, which indicates that the method used to determine the concentration of salt within a sample works as intended. The lower concentration of salt determined in sample HS may be attributed to the fact that this sample had whole flakes of salt crystals within the lipid matrix; hence the average concentration in the droplets is expected to be lower than what is listed for the sample. The high salt concentration determined for the sample NS-5 is thought to be due to the low quality of the images used for the analysis. The high concentration of salt determined for the NS-4 sample may be due to the laser not reaching the desired intensity for a major part of the images. Upon reviewing figure 4.26, it can be seen that a small amount of the data-points seem to cluster around 10w% salt, while the

majority of the data-points are seen to cluster around 20w% salt. This split is observed in the results from even a single image; hence the laser power did not change. This may indicate an incomplete mixing of the salt-slurry that has been added to the butter.

In general, a slightly lower concentration of salt has been determined compared to what is actually present in the samples. This may be corrected by doing more measurements, to which the calibration can be fitted. Another possibility that must not be ignored is the very different nature of the samples which are used for the calibration of the dataanalysis and the actual samples measured on. The calibration was done on homogenous samples of water, where images were acquired relatively far from any edges that could affect the coordination of water molecules. In comparison, the actual images are of droplets of water, inside a highly scattering environment. The effects of an edge will be more pronounced in very small droplets (less volume per surface area); hence the lower limit for droplets considered during the dataanalysis may be adjusted to enhance precision of the analysis.

In contrast to this, the effects that the largest droplets have on the results may also be considered. Larger droplets show the same tendency for all samples (except for the NS-3): the larger the droplet, the lower the determined concentration of salt. Some of the larger droplets have been determined to have a lower concentration of salt, which indicate that the whole sample may not have been stirred enough to have become completely homogenous. Furthermore it was attempted to take the scattering effects of the samples of butter into account, by preparing well defined and simple samples with known concentrations of salt and perform calibrative measurements on them. It was, however, not possible to obtain useful images of these samples.

Chapter 6

Conclusion

The SRS-microscope was built and characterized, though it did not prove possible to make it capable of acquiring images of a useful quality. It was possible to determine the optimal incident power on the detector used in the SRS-setup to be around 125mW. If the detector is illuminated by more than 250mW, the detector becomes saturated and a proper SRS-signal cannot be distinguished by the lock-in amplifier. It was determined that the bias on the detector should be as large as possible to improve the temporal resolution of the detector. The lock-in amplifier was shown to work as intended and it was observed that most of the noise in the SRS-images was picked up in the ADC, why it must be moved away from any nearby sources of noise, for the quality of the SRS-images to improve. Furthermore the two laser-beams were found to not be optimally aligned in the z-direction, making the acquisition of high quality images by both CARS and SRS impossible. In the future it may prove useful to create a program that can automatically adjust the settings of the microscope and the lock-in amplifier in the most favorable way for the acquisition of SRS-images.

The method used to determine the concentration of salt in butter was proven to work for the forward-detected images. The epifluorescence-detected images may need a different calibration to be useful, though the attempt to test and calibrate the system to model-systems of butter proved to not work, as the model systems either did not resemble butter on a microscopic scale or melted too fast for images to be acquired. To increase the speed of the analysis, the next logic step is to implement parallel processing when analyzing the images.

It was shown that the dataanalysis was able to provide qualitative information on how the different samples were prepared relative to each other, even though the imperfect tuning-process of the laser made the data-acquisition laborious and demanded the addition of a sorting algorithm to the automated analysis. In the future, to make sure that the laser had reached the desired intensity, the output intensity may be measured manually or more images may be acquired of the same spot within a sample, to be able to identify and remove images that are obtained with a different laser intensity.

Bibliography

- [1] P. T. C. So, C. Y. Dong, B. R. Masters, and K. M. Berland, “Two-Photon Excitation Fluorescence Microscopy,” *Annu. Rev. Biomed. Eng.*, vol. 2, pp. 399–429, aug 2000.
- [2] C. W. Freudiger, W. Min, B. G. Saar, S. Lu, G. R. Holtom, C. He, J. C. Tsai, J. X. Kang, and X. S. Xie, “Label-Free Biomedical Imaging with High Sensitivity by Stimulated Raman Scattering Microscopy,” in *Hawley’s Condens. Chem. Dict.*, vol. 275, pp. 1934–1937, Hoboken, NJ, USA: John Wiley & Sons, Inc., mar 2007.
- [3] B. G. Saar, L. R. Contreras-Rojas, X. S. Xie, and R. H. Guy, “Imaging drug delivery to skin with stimulated raman scattering microscopy,” *Mol. Pharm.*, vol. 8, no. 3, pp. 969–975, 2011.
- [4] B. G. Saar, R. S. Johnston, C. W. Freudiger, X. S. Xie, and E. J. Seibel, “Coherent Raman scanning fiber endoscopy,” *Opt. Lett.*, vol. 36, no. 13, p. 2396, 2011.
- [5] W. W. Denk, J. H. Strickler, “Two-Photon Laser Scanning Fluorescence Microscopy,” *Science (80-.)*, vol. 248, no. 4951, pp. 73–76, 1990.
- [6] B. G. Saar, C. W. Freudiger, J. Reichman, C. M. Stanley, R. Holtom, X. S. Xie, G. R. Holtom, and X. S. Xie, “Video-Rate Molecular Imaging in Vivo with Stimulated Raman Scattering,” vol. 330, no. 6009, pp. 1368–1370, 2010.
- [7] J. H. Hibben, “The Raman Spectra of Water, Aqueous Solutions and Ice,” *J. Chem. Phys.*, vol. 5, no. 3, p. 166, 1937.
- [8] D. M. Carey and G. M. Korenowski, “Measurement of the Raman spectrum of liquid water,” *J. Chem. Phys.*, vol. 108, no. 7, pp. 2669–2675, 1998.
- [9] R. Li, Z. Jiang, Y. Guan, H. Yang, and B. Liu, “Effects of metal ion on the water structure studied by the Raman O-H stretching spectrum,” *J. Raman Spectrosc.*, vol. 40, no. 9, pp. 1200–1204, 2009.
- [10] J. X. Cheng and X. S. Xie, *Coherent Raman Scattering Microscopy*. CRC Press, 2012.
- [11] C. V. RAMAN and K. S. KRISHNAN, “A New Type of Secondary Radiation,” *Nature*, vol. 121, pp. 501–502, mar 1928.

- [12] G. Placzek, *Handbuch der Radiologie*. Leipzig, Germany: Akademische Verlagsgesellschaft, 1934.
- [13] Stanford Research Systems, “About Lock-In Amplifiers,” *Appl. Note*, no. 408, pp. 1–9, 2011.
- [14] Zürich Instruments, “White Paper: Principles of lock-in detection and the state of the art Zurich Instruments,” *White Pap.*, no. November, pp. 1–10, 2016.
- [15] Lehigh University, “Lock - in Amplifier and Applications,” tech. rep., 2008.
- [16] T. Edition, *Fundamentals of Dairy Chemistry*. Boston, MA: Springer US, 1995.
- [17] G. Elert, “Density - The Physics Hypertextbook.”
- [18] L. Pauling, “The Structure and Entropy of Ice and of Other Crystals with Some Randomness of Atomic Arrangement,” *J. Am. Chem. Soc.*, vol. 57, no. 12, pp. 2680–2684, 1935.
- [19] P. C. Cross, J. Burnham, and P. A. Leighton, “The Raman Spectrum and the Structure of Water,” *J. Am. Chem. Soc.*, vol. 59, no. 6, pp. 1134–1147, 1937.
- [20] M. Ahmed, V. Namboodiri, A. K. Singh, J. A. Mondal, and S. K. Sarkar, “How ions affect the structure of water: A combined raman spectroscopy and multivariate curve resolution study,” *J. Phys. Chem. B*, vol. 117, no. 51, pp. 16479–16485, 2013.
- [21] I. Duričković, M. Marchetti, R. Claverie, P. Bourson, J.-M. Chassot, and M. D. Fontana, “Experimental Study of NaCl Aqueous Solutions by Raman Spectroscopy: Towards a New Optical Sensor,” *Appl. Spectrosc.*, vol. 64, pp. 853–857, aug 2010.
- [22] J. B. Ding, K. T. Takasaki, and B. L. Sabatini, “Supraresolution Imaging in Brain Slices using Stimulated-Emission Depletion Two-Photon Laser Scanning Microscopy,” *Neuron*, vol. 63, pp. 429–437, aug 2009.
- [23] Anfatec, “eLockIn 205/2,” Tech. Rep. 0, Anfatec, Oelsnitz /V., 2014.
- [24] Wikipedia, “Transistor-transistor logic,” 2017.
- [25] Thorlabs, “Mounted Si Photodiode,” pp. 1–4, 2012.
- [26] N. Otsu, “A Threshold Selection Method from Gray-Level Histograms,” *IEEE Trans. Syst. Man. Cybern.*, vol. 9, no. 1, pp. 62–66, 1979.
- [27] P. Nandakumar, A. Kovalev, and A. Volkmer, “Vibrational imaging based on stimulated Raman scattering microscopy,” *New J. Phys.*, vol. 11, p. 033026, mar 2009.

Chapter 7

Appendix

In the following chapter is brought all appendices referred to in earlier chapters.

7.1 Appendix I

The following section holds all plots of results based on epifluorescent-detected images.

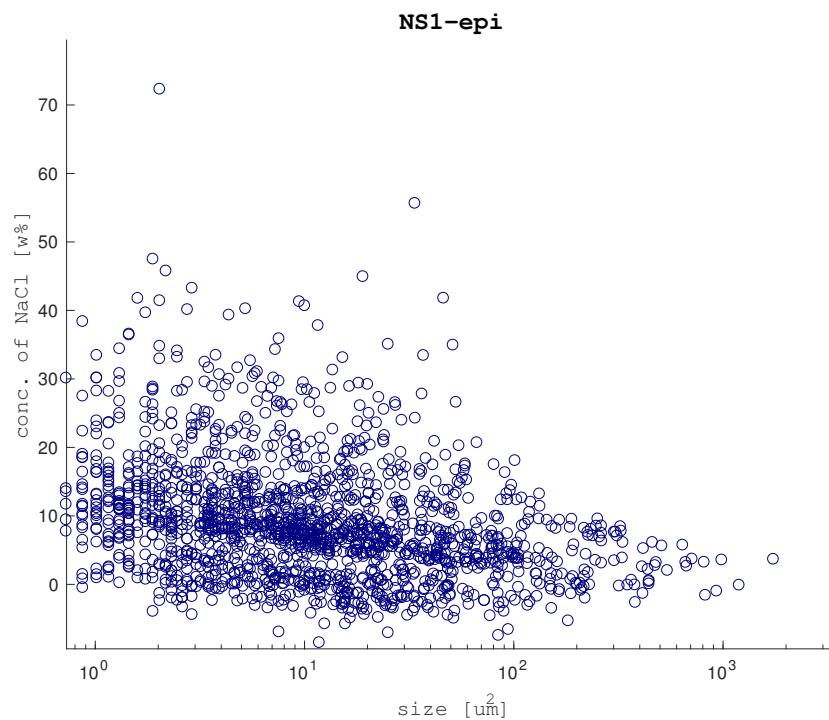


Figure 7.1: Plot of results from epifluorescent-detected images of sample NS-1.

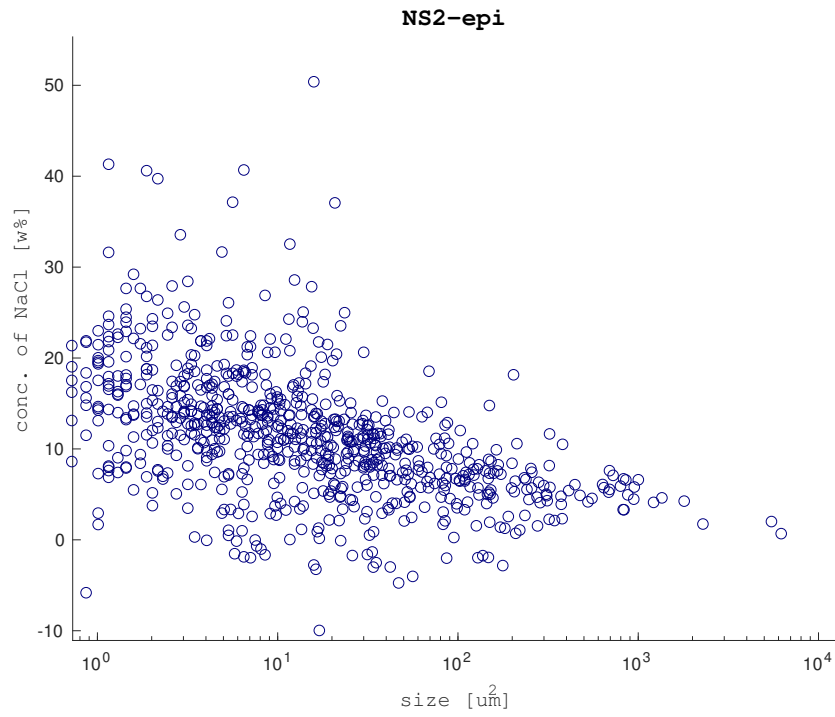


Figure 7.2: Plot of results from epifluorescent-detected images of sample NS-2.

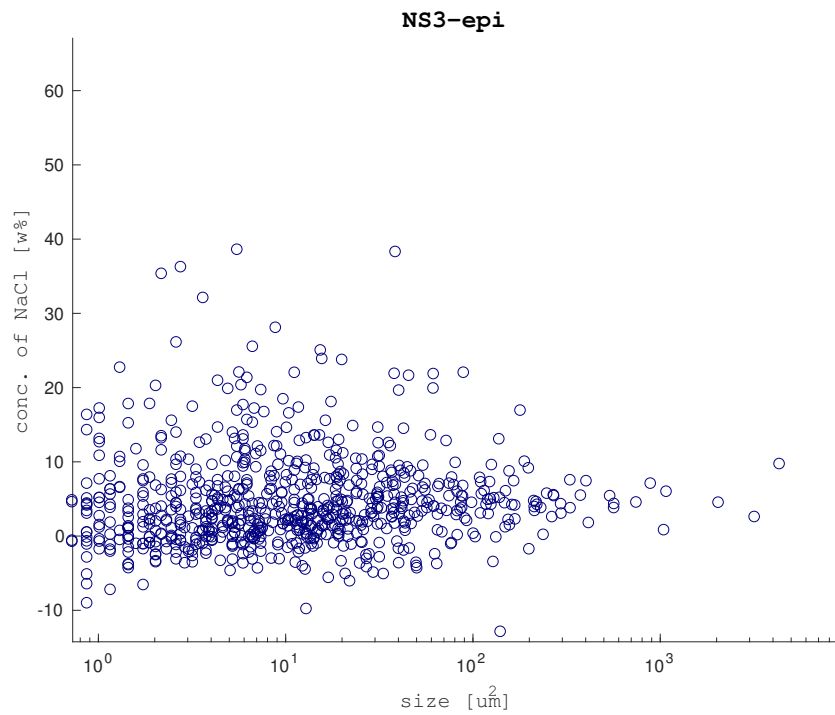


Figure 7.3: Plot of results from epifluorescent-detected images of sample NS-3.

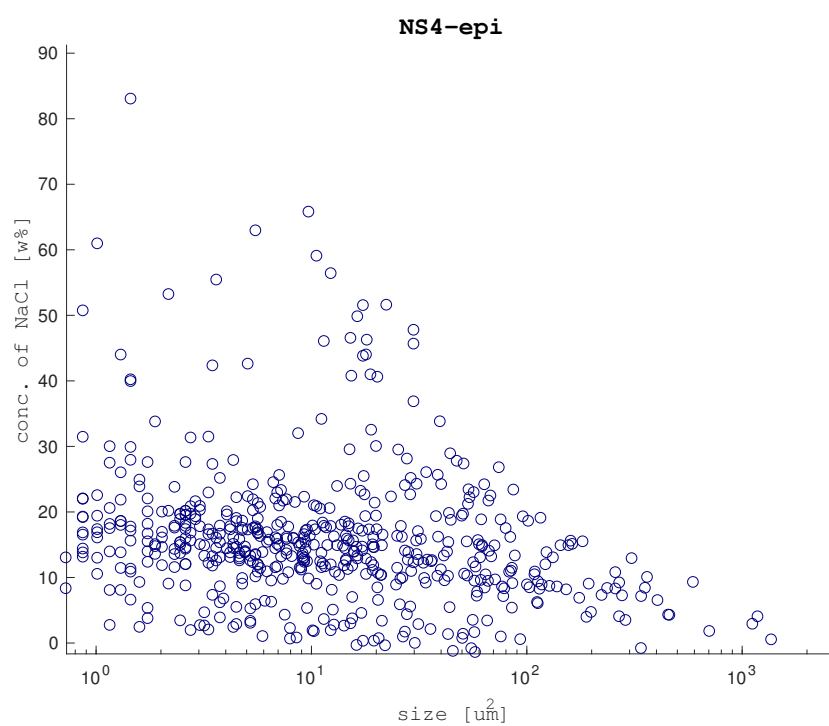


Figure 7.4: Plot of results from epifluorescent-detected images of sample NS-4 (organic).

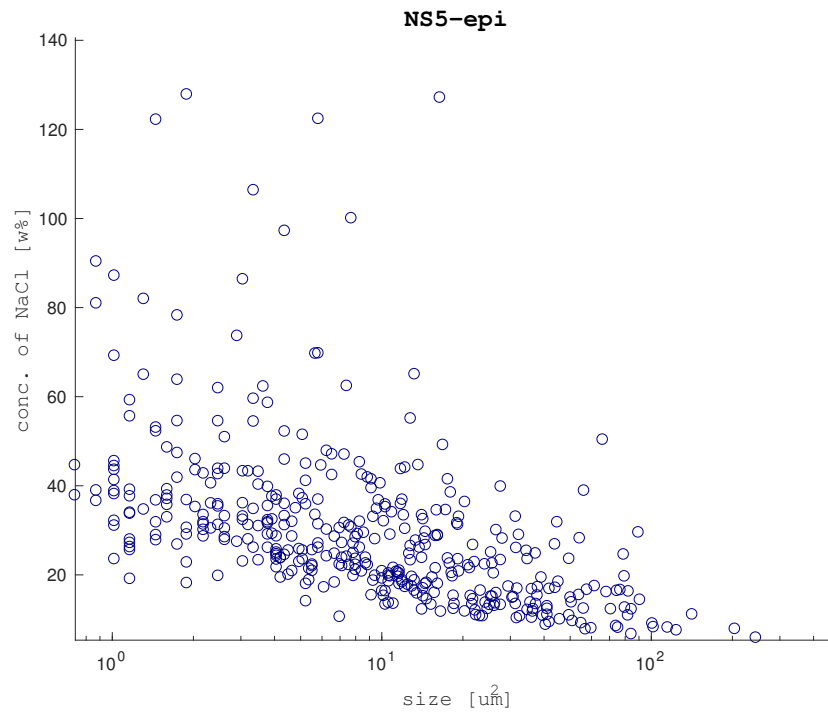


Figure 7.5: Plot of results from epifluorescent-detected images of sample NS-4 (25% vegetable oil).

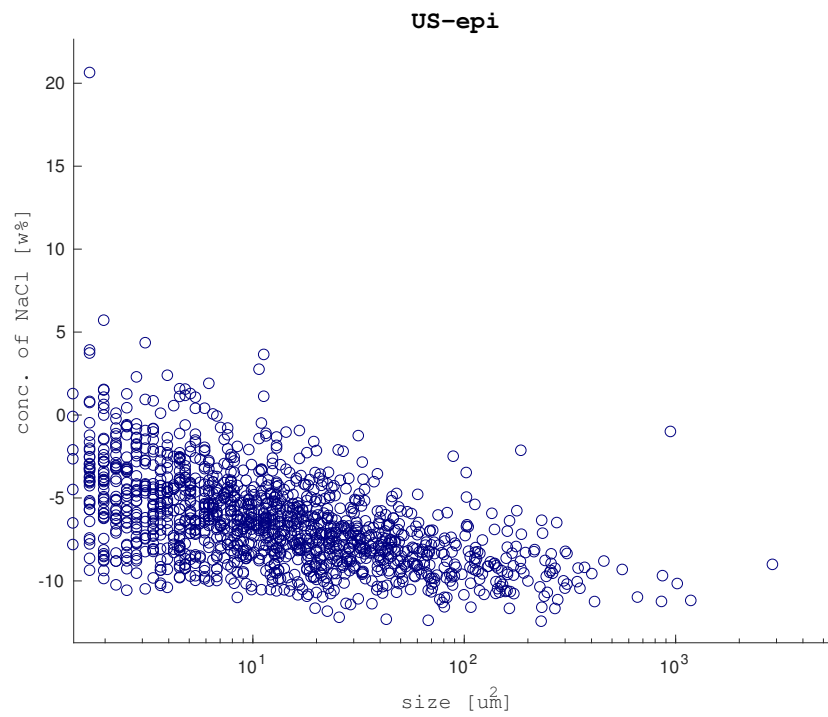


Figure 7.6: Plot of results from epifluorescent-detected images of sample US.

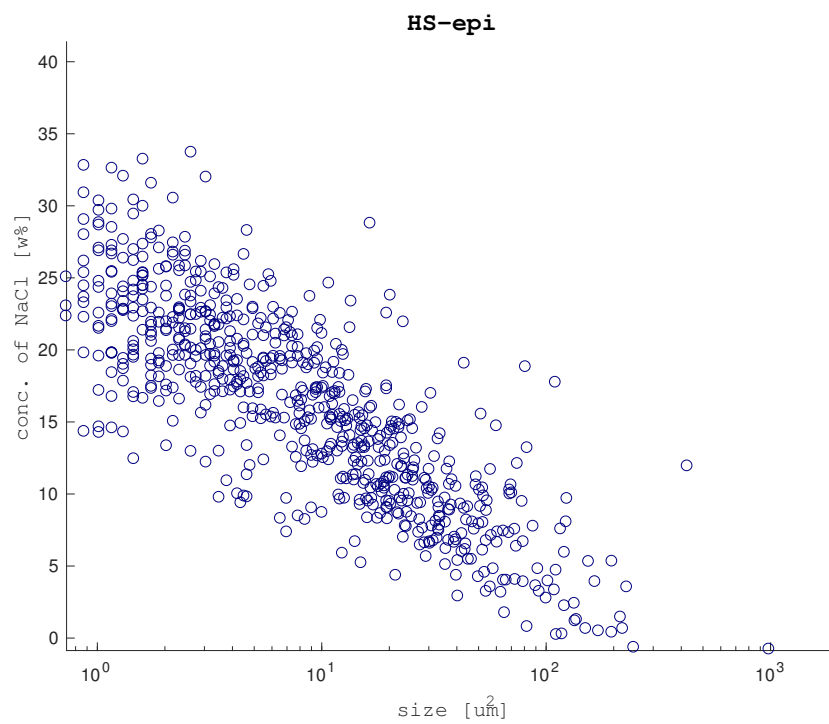


Figure 7.7: Plot of results from epifluorescent-detected images of sample HS.

7.2 Protocol: Imaging of Aqueous Solutions of Ions for Calibration

The following section will cover the datastructure and naming of files that are necessary for the calibration-script, developed during this project to determine a relation between CARS-signals of water at two wavenumbers and the concentration of NaCl in aqueous solutions, to function. Furthermore the protocol will describe how to take proper images to be used for the calibration.

7.2.1 Datastructure and Filenaming

The script used for dataanalysis is independent with regard to placement of files to be analyzed. The user only needs to choose the files through a Matlab-filebrowser that pops up when the script is run. It is advised to store all images according to the structure: *date/images/*, where the images to be analysed are stored inside the folder *images*. The script will use this structure to automatically name and place files created during the analysis.

The script expects all image-files to be of the *.tif*-format and named according to *wavelength-iretake.tif*, where wavelength is either 785 or 795, the *i* is a number that represents a unique location within the sample and "retake" can be one of the letters: *A, B, C, D or E*. . Each file is expected to contain two images: the first being the forward-detected image and the second being the epifluorescence-detected image.

All files created during the analysis are placed in the folder *date/*. The script will create and save a plot of the detected intensity against the known concentration of salt, which is done for both directions of detection. Furthermore a *.csv*-file *bad_data_sets.csv* listing all the images that did not produce results within the allowed deviance is saved for the most recent analysis of the specific sample. The results of the calibration can be observed from the legend of the plots.

The script expect the file *salt_concentrations.mat* to be present in the folder *date/* and to be a row-vector containing the concentrations of salt in the samples that are analyzed.

7.2.2 Imaging

All images are acquired using CARS to probe the wavenumbers 3180cm^{-1} and 3340cm^{-1} , which on the system that the script was developed for are equal to 795nm and 785nm respectively, when a 1064nm Stokes laser is used. Every image is acquired five times at one position, starting at 795nm, after which the laser is tuned to the other wavelength and another five images are acquired. This is done for five different locations within each sample.

All images should be acquired at a distance to the glass/water-interface at the bottom of the microscope-well and at the same settings for laser power and detector bias. One possible setting is: forward-detector at 550V bias and epifluorescence-detector at 680V bias, with the laser power set to: 67% of 900mW pump and 81% of 1300mW Stokes.

Prior to measurements, the offset of the detectors should be adjusted accordingly.

7.3 Protocol: Imaging of Butter for Calculation of Concentration of Salt

The following section will cover how the datastructure and naming of files that are necessary for the analysis-script developed during this project to function.

7.3.1 Datastructure and Filenaming

The script used for dataanalysis is independent with regard to placement of files to be analyzed. The user only needs to choose the files through a Matlab-filebrowser that pops up when the script is run. It is advised to store all images according to the structure: *samplename/date/images/*, where the images to be analysed are stored inside the folder *images*. The script will use this structure to automatically name and place files created during the analysis.

The script expects all image-files to be of the *.tif*-format and named according to *wavelength-retake.tif*, where wavelength is either *785* or *795* and "retake" can be one of the letters: *A, B, C, D* or *E*, representing a unique location within the sample. Each file is expected to contain two images: the first being the forward-detected image and the second being the epifluorescence-detected image.

All files created during the analysis are placed in the folder *samplename/date/*. The script will create and save a plot of determined concentrations of salt against the size of the droplets, which is done for both directions of detection. Furthermore a *.csv*-file *analysed_images.csv* listing all the images were used during the analysis is saved for the most recent analysis of the specific sample as well as a file *results.txt* listing the determined values for the sample.

7.3.2 Imaging

When imaging samples of butter, it is important to start with an ax-scan to determine the z-position that yields the greatest signal from the sample. When this position is determined, the imaging in the xy-plane can begin. All images are acquired using CARS to probe the wavenumbers 3180cm^{-1} and 3340cm^{-1} , which on the system that the script was developed for are equal to 795nm and 785nm respectively, when a 1064nm Stokes laser is used. Every image is acquired once for each wavenumber, at five different locations within the sample.

All images should be acquired using the same settings as were used when acquiring images for the calibration. When acquiring the images, droplets that are out-of-focus will be present in the image. It is advised to shift the focus to a different location within the sample to avoid the out-of-focus droplets, as they may not be properly illuminated and therefore give off a signal that is not representative of the concentration of salt within the droplet.

7.4 Script: Dataanalysis in Matlab for Calibration of Intensity of Raman Signal for Aqueous Solutions of Ions

```
1 % By Brian Bjarke Jensen (brjen12@student.sdu.dk)
   20/11-2017
2 clearvars
3 disp('waiting for input');
4
5 % Setting allowed deviances for measurements
6 allowed_deviance_3340_for = 0.1; % Based on
   preliminary measurements
7 allowed_deviance_3340_epi = 0.1; % Based on
   preliminary measurements
8 allowed_deviance_3180_for = 0.08; % Based on
   preliminary measurements
9 allowed_deviance_3180_epi = 0.025; % Based on
   preliminary measurements
10
11 % Import and read images
12 [filenames, path] = uigetfile('*.tif', 'Choose Images'
   , 'Multiselect', 'on');
13 save_path = strsplit(path, '/');
14 save_path = strjoin(save_path(1:end-2), '/');
15 save_path = strcat(save_path, '/');
16 disp('reading images');
17 a = 1; I_3340_tags = []; b = 1; I_3180_tags = [];
18 for i = 1:length(filenames)
19     filename = strsplit(filenames{i}, '-');
20     sample = str2double(filename{1});
21     wavelength = str2double(filename{2});
22     location = str2double(filename{3}(1));
23     retake = filename{3}(2);
24     switch retake
25         case 'A'
26             retake = 1;
27         case 'B'
28             retake = 2;
29         case 'C'
30             retake = 3;
31         case 'D'
32             retake = 4;
33         case 'E'
34             retake = 5;
35         otherwise
36             disp('ERROR: one or more filenames did not
               meet protocol naming standard: retakes
               in name');
37             return
38     end
39     if wavelength == 785
40         I_3340_for{sample, location, retake} = imread(
               strcat(path, filenames{i}), 1);
```

```
41     I_3340_epi{sample, location, retake} = imread(  
42         strcat(path, filenames{i}), 2);  
43     I_3340_tags(a, 1) = i;  
44     a = a + 1;  
45     elseif wavelength == 795  
46         I_3180_for{sample, location, retake} = imread(  
47             strcat(path, filenames{i}), 1);  
48         I_3180_epi{sample, location, retake} = imread(  
49             strcat(path, filenames{i}), 2);  
50         I_3180_tags(b, 1) = i;  
51         b = b + 1;  
52     else  
53         disp('ERROR: one or more filenames did not  
54             meet protocol naming standard: wavelength  
55             in name');  
56         return  
57     end  
58 end  
59 clearvars i filename sample wavelength location retake  
60 a b  
61 % Check that images satisfy protocol standard  
62 if ~exist('I_3340_for') | ~exist('I_3340_epi') | ~  
63     exist('I_3180_for') | ~exist('I_3180_epi')  
64     disp('ERROR: one or more image types were not  
65         provided');  
66     return  
67 end  
68 if length(I_3340_for) ~= length(I_3180_for) | length(  
69     I_3340_epi) ~= length(I_3180_epi)  
70     disp('ERROR: uneven number of images')  
71     return  
72 end  
73 for i = 1:length(I_3340_for)  
74     if size(I_3340_for{i}) ~= size(I_3180_for{i}) |  
75         size(I_3340_epi{i}) ~= size(I_3180_epi{i})  
76         disp('ERROR: one or more images are the same  
77             size');  
78         return  
79     end  
80 end  
81 % Load concentration of salt  
82 salt_file = strcat(save_path, 'salt_concentrations.mat  
83     ');  
84 if exist(salt_file) == 2  
85     load(salt_file);  
86 else  
87     disp('no salt_concentrations.mat-file was located  
88         in this folder');
```

```
78     salt_conc = input('please input concentrations of
79     salt as "[c1; c2; c3; ... cn]": ');
80     if isempty(salt_conc)
81         disp('ERROR: no salt concentration(s) provided
82         ');
83         return
84     end
85     end
86     end
87     % Calculate mean intensity of images
88     disp('calculating mean intensities of images');
89     [samples, locations, retakes] = size(I_3340_for);
90     for sample = 1:samples
91         for location = 1:locations
92             for retake = 1:retakes
93                 mean_retakes{sample, location}(retake) =
94                 mean(mean(I_3340_for{sample, location,
95                 retake}));
96             end
97             mean_locations_3340_for{sample}(location) =
98             mean(mean_retakes{sample, location});
99         end
100     end
101     clearvars I_3340_for
102     [samples, locations, retakes] = size(I_3340_epi);
103     for sample = 1:samples
104         for location = 1:locations
105             for retake = 1:retakes
106                 mean_retakes{sample, location}(retake) =
107                 mean(mean(I_3340_epi{sample, location,
108                 retake}));
109             end
110             mean_locations_3340_epi{sample}(location) =
111             mean(mean_retakes{sample, location});
112         end
113     end
114     clearvars I_3180_for
115     [samples, locations, retakes] = size(I_3180_for);
116     for sample = 1:samples
117         for location = 1:locations
118             for retake = 1:retakes
119                 mean_retakes{sample, location}(retake) =
120                 mean(mean(I_3180_for{sample, location,
121                 retake}));
122             end
123             mean_locations_3180_for{sample}(location) =
124             mean(mean_retakes{sample, location});
125         end
126     end
127     clearvars I_3180_for
```

```
117 [samples, locations, retakes] = size(I_3180_epi);
118 for sample = 1:samples
119     for location = 1:locations
120         for retake = 1:retakes
121             mean_retakes{sample, location}(retake) =
                mean(mean(I_3180_epi{sample, location,
                    retake}));
122         end
123         mean_locations_3180_epi{sample}(location) =
                mean(mean_retakes{sample, location});
124     end
125 end
126 clearvars I_3180_epi
127 clearvars sample samples location locations retake
        retakes mean_retakes
128
129 % Remove bad data - 3340-for
130 bad_data_tags = []; bad_data_counter = 1;
131 disp('removing bad data');
132 test_x = reshape(repmat(salt_conc, 1, 5).', [], 1);
133 test_y = cell2mat(mean_locations_3340_for).';
134 tags = cell2mat(filenamees(I_3340_tags(1:5:end)).');
135 tags = tags(:,1:7);
136 test_fit = polyfit(test_x, test_y, 1);
137 plot_title = strsplit(save_path, '/');
138 plot_title = char(plot_title{end-1});
139 fig = figure;
140 hold on
141 hTitle = title(strcat(plot_title, '-3340-for not
        filtered for bad data'));
142 plot(test_x, test_y, 'o');
143 plot([min(test_x), max(test_x)], test_fit(1) .* [min(
        test_x), max(test_x)] + test_fit(2));
144 xlabel('concentration of NaCl [w%]');
145 ylabel('intensity [a.u.]');
146 hold off
147 test_diff = abs((test_fit(1) .* test_x + test_fit(2))
        - test_y);
148 [max_diff, max_diff_index] = max(test_diff);
149 limit = abs((test_fit(1) .* test_x(max_diff_index) -
        test_fit(2))) * allowed_deviance_3340_for;
150 while max_diff > limit
151     bad_data_tags{bad_data_counter} = [tags(
        max_diff_index, :)];
152     tags(max_diff_index, :) = '';
153     bad_data_counter = bad_data_counter + 1;
154     test_x(max_diff_index) = [];
155     test_y(max_diff_index, :) = [];
156     test_fit = polyfit(test_x, test_y, 1);
```

```
157     test_diff = abs((test_fit(1) .* test_x + test_fit
158         (2)) - test_y);
159     [max_diff, max_diff_index] = max(test_diff);
160 end
161 fig = figure;
162 hold on
163 hTitle = title(strcat(plot_title, '-3340-for filtered
164     for bad data'));
165 plot(test_x, test_y, 'o');
166 plot([min(test_x), max(test_x)], test_fit(1) .* [min(
167     test_x), max(test_x)] + test_fit(2));
168 xlabel('concentration of NaCl [w%]');
169 ylabel('intensity [a.u.]');
170 hold off
171 clearvars mean_locations_3340_for
172 for i = 1:length(test_y)
173     sample = str2num(tags(i, 1));
174     location = str2num(tags(i, end));
175     salt_3340_for(sample) = salt_conc(sample);
176     mean_locations_3340_for{sample}(location) = test_y
177         (i);
178 end
179 for i = 1:length(mean_locations_3340_for)
180     [y, x] = size(mean_locations_3340_for{i});
181     if y ~= 0
182         indices = mean_locations_3340_for{i} == 0;
183         mean_locations_3340_for{i}(indices) = [];
184     end
185 end
186 % Remove bad data - 3340-epi
187 test_x = reshape repmat(salt_conc, 1, 5).', [], 1);
188 test_y = cell2mat(mean_locations_3340_epi).';
189 tags = cell2mat(filename(I_3340_tags(1:5:end))).';
190 tags = tags(:,1:7);
191 test_fit = polyfit(test_x, test_y, 1);
192 fig = figure;
193 hold on
194 hTitle = title(strcat(plot_title, '-3340-epi not
195     filtered for bad data'));
196 plot(test_x, test_y, 'o');
197 plot([min(test_x), max(test_x)], test_fit(1) .* [min(
198     test_x), max(test_x)] + test_fit(2));
199 xlabel('concentration of NaCl [w%]');
200 ylabel('intensity [a.u.]');
201 hold off
202 test_diff = abs((test_fit(1) .* test_x + test_fit(2))
203     - test_y);
204 [max_diff, max_diff_index] = max(test_diff);
```

```

199 limit = abs((test_fit(1) .* test_x(max_diff_index) -
200 test_fit(2))) * allowed_deviance_3340_epi;
201 while max_diff > limit
202     bad_data_tags{bad_data_counter} = [tags(
203         max_diff_index, :)];
204     tags(max_diff_index, :) = '';
205     bad_data_counter = bad_data_counter + 1;
206     test_x(max_diff_index) = [];
207     test_y(max_diff_index, :) = [];
208     test_fit = polyfit(test_x, test_y, 1);
209     test_diff = abs((test_fit(1) .* test_x + test_fit
210         (2)) - test_y);
211     [max_diff, max_diff_index] = max(test_diff);
212 end
213 fig = figure;
214 hold on
215 hTitle = title(strcat(plot_title, '-3340-epi filtered
216     for bad data'));
217 plot(test_x, test_y, 'o');
218 plot([min(test_x), max(test_x)], test_fit(1) .* [min(
219     test_x), max(test_x)] + test_fit(2));
220 xlabel('concentration of NaCl [w%]');
221 ylabel('intensity [a.u.]');
222 hold off
223 clearvars mean_locations_3340_epi
224 for i = 1:length(test_y)
225     sample = str2num(tags(i, 1));
226     location = str2num(tags(i, end));
227     salt_3340_epi(sample) = salt_conc(sample);
228     mean_locations_3340_epi{sample}(location) = test_y
229         (i);
230 end
231 for i = 1:length(mean_locations_3340_epi)
232     [y, x] = size(mean_locations_3340_epi{i});
233     if y ~= 0
234         indices = mean_locations_3340_epi{i} == 0;
235         mean_locations_3340_epi{i}(indices) = [];
236     end
237 end
238 end
239 % Remove bad data - 3180-for
240 test_x = reshape(repmat(salt_conc, 1, 5).', [], 1);
241 test_y = cell2mat(mean_locations_3180_for).';
242 tags = cell2mat(filenamees(I_3180_tags(1:5:end)).');
243 tags = tags(:,1:7);
244 test_fit = polyfit(test_x, test_y, 1);
245 fig = figure;
246 hold on
247 hTitle = title(strcat(plot_title, '-3180-for not
248     filtered for bad data'));

```

```
242 plot(test_x, test_y, 'o');
243 plot([min(test_x), max(test_x)], test_fit(1) .* [min(
    test_x), max(test_x)] + test_fit(2));
244 xlabel('concentration of NaCl [w%]');
245 ylabel('intensity [a.u.]');
246 hold off
247 test_diff = abs((test_fit(1) .* test_x + test_fit(2))
    - test_y);
248 [max_diff, max_diff_index] = max(test_diff);
249 limit = abs((test_fit(1) .* test_x(max_diff_index) -
    test_fit(2))) * allowed_deviance_3180_for;
250 while max_diff > limit
251     bad_data_tags{bad_data_counter} = [tags(
        max_diff_index, :)];
252     tags(max_diff_index, :) = '';
253     bad_data_counter = bad_data_counter + 1;
254     test_x(max_diff_index) = [];
255     test_y(max_diff_index, :) = [];
256     test_fit = polyfit(test_x, test_y, 1);
257     test_diff = abs((test_fit(1) .* test_x + test_fit
        (2)) - test_y);
258     [max_diff, max_diff_index] = max(test_diff);
259 end
260 fig = figure;
261 hold on
262 hTitle = title(strcat(plot_title, '-3180-for filtered
    for bad data'));
263 plot(test_x, test_y, 'o');
264 plot([min(test_x), max(test_x)], test_fit(1) .* [min(
    test_x), max(test_x)] + test_fit(2));
265 xlabel('concentration of NaCl [w%]');
266 ylabel('intensity [a.u.]');
267 hold off
268 clearvars mean_locations_3180_for
269 for i = 1:length(test_y)
270     sample = str2num(tags(i, 1));
271     location = str2num(tags(i, end));
272     salt_3180_for(sample) = salt_conc(sample);
273     mean_locations_3180_for{sample}(location) = test_y
        (i);
274 end
275 for i = 1:length(mean_locations_3180_for)
276     [y, x] = size(mean_locations_3180_for{i});
277     if y ~= 0
278         indices = mean_locations_3180_for{i} == 0;
279         mean_locations_3180_for{i}(indices) = [];
280     end
281 end
282
283 % Remove bad data - 3180-epi
```

```

284 test_x = reshape(repmat(salt_conc, 1, 5).', [], 1);
285 test_y = cell2mat(mean_locations_3180_epi).';
286 tags = cell2mat(filenamees(I_3180_tags(1:5:end)).');
287 tags = tags(:,1:7);
288 test_fit = polyfit(test_x, test_y, 1);
289 fig = figure;
290 hold on
291 hTitle = title(strcat(plot_title, '-3180-epi not
    filtered for bad data'));
292 plot(test_x, test_y, 'o');
293 plot([min(test_x), max(test_x)], test_fit(1) .* [min(
    test_x), max(test_x)] + test_fit(2));
294 xlabel('concentration of NaCl [w%]');
295 ylabel('intensity [a.u.]');
296 hold off
297 test_diff = abs((test_fit(1) .* test_x + test_fit(2))
    - test_y);
298 [max_diff, max_diff_index] = max(test_diff);
299 limit = abs((test_fit(1) .* test_x(max_diff_index) -
    test_fit(2))) * allowed_deviance_3180_epi;
300 while max_diff > limit
301     bad_data_tags{bad_data_counter} = [tags(
        max_diff_index, :)];
302     tags(max_diff_index, :) = '';
303     bad_data_counter = bad_data_counter + 1;
304     test_x(max_diff_index) = [];
305     test_y(max_diff_index, :) = [];
306     test_fit = polyfit(test_x, test_y, 1);
307     test_diff = abs((test_fit(1) .* test_x + test_fit
        (2)) - test_y);
308     [max_diff, max_diff_index] = max(test_diff);
309 end
310 fig = figure;
311 hold on
312 hTitle = title(strcat(plot_title, '-3180-epi filtered
    for bad data'));
313 plot(test_x, test_y, 'o');
314 plot([min(test_x), max(test_x)], test_fit(1) .* [min(
    test_x), max(test_x)] + test_fit(2));
315 xlabel('concentration of NaCl [w%]');
316 ylabel('intensity [a.u.]');
317 hold off
318 clearvars mean_locations_3180_epi
319 for i = 1:length(test_y)
320     sample = str2num(tags(i, 1));
321     location = str2num(tags(i, end));
322     salt_3180_epi(sample) = salt_conc(sample);
323     mean_locations_3180_epi{sample}(location) = test_y
        (i);
324 end

```

```
325 for i = 1:length(mean_locations_3180_epi)
326     [y, x] = size(mean_locations_3180_epi{i});
327     if y ~= 0
328         indices = mean_locations_3180_epi{i} == 0;
329         mean_locations_3180_epi{i}(indices) = [];
330     end
331 end
332 bad_data_sets = char(bad_data_tags);
333 clearvars bad_data_counter limit max_diff
334     max_diff_index tags test_diff test_fit test_x
335     test_y indices bad_data_tags
336
337 % Calculate mean and standard deviation
338 a = 1;
339 for i = 1:length(mean_locations_3340_for)
340     result = mean(mean_locations_3340_for{i});
341     if ~isnan(result)
342         mean_3340_for(a) = result;
343         SD_3340_for(a) = std(mean_locations_3340_for{i}
344             );
345         a = a + 1;
346     else
347         salt_3340_for(i) = [];
348     end
349 end
350 a = 1;
351 for i = 1:length(mean_locations_3340_epi)
352     result = mean(mean_locations_3340_epi{i});
353     if ~isnan(result)
354         mean_3340_epi(a) = result;
355         SD_3340_epi(a) = std(mean_locations_3340_epi{i}
356             );
357         a = a + 1;
358     else
359         salt_3340_epi(i) = [];
360     end
361 end
362 a = 1;
363 for i = 1:length(mean_locations_3180_for)
364     result = mean(mean_locations_3180_for{i});
365     if ~isnan(result)
366         mean_3180_for(a) = result;
367         SD_3180_for(a) = std(mean_locations_3180_for{i}
368             );
369         a = a + 1;
370     else
371         salt_3180_for(i) = [];
372     end
373 end
```

```
370 a = 1;
371 for i = 1:length(mean_locations_3180_epi)
372     result = mean(mean_locations_3180_epi{i});
373     if ~isnan(result)
374         mean_3180_epi(a) = result;
375         SD_3180_epi(a) = std(mean_locations_3180_epi{i}
376                               });
376         a = a + 1;
377     else
378         salt_3180_epi(i) = [];
379     end
380 end
381 clearvars a
382
383 % Calculate linear fits
384 disp('calculating linear fits');
385 fit_3340_for = polyfit(salt_3340_for(:), mean_3340_for
386                       (:), 1);
387 fit_3340_for_x = [min(salt_3340_for(:)), max(
388                   salt_3340_for(:))];
389 fit_3340_for_y = fit_3340_for(1) .* fit_3340_for_x +
390                 fit_3340_for(2);
391 fit_3340_epi = polyfit(salt_3340_epi(:), mean_3340_epi
392                       (:), 1);
393 fit_3340_epi_x = [min(salt_3340_epi(:)), max(
394                   salt_3340_epi(:))];
395 fit_3340_epi_y = fit_3340_epi(1) .* fit_3340_epi_x +
396                 fit_3340_epi(2);
397
398 % Plot for-results
399 disp('plotting results');
400 plot_title = strsplit(save_path, '/');
401 plot_title = char(plot_title{end-1});
402 plot_title = strcat(plot_title, '-saltcalibration-', '
403                       for');
404 fig = figure;
405 hold on
406 ax = gca;
```

```

406 set(ax, 'FontName', 'Helvetica');
407 hTitle = title('saltcalibration');
408 set(hTitle, 'FontSize', 12, 'FontWeight', 'bold');
409 hXLabel = xlabel('concentration of NaCl [w%]');
410 hYLabel = ylabel('intensity [a.u.]');
411 set([hXLabel, hYLabel], 'FontSize', 10);
412 set([hTitle, hXLabel, hYLabel], 'FontName', '
    AvantGarde');
413 hData_3340 = errorbar(salt_3340_for(:), mean_3340_for
    (:), SD_3340_for(:), 'o', 'Color', [0, 0, 0.5]);
414 hFit_3340 = plot(fit_3340_for_x, fit_3340_for_y);
415 hData_3180 = errorbar(salt_3180_for(:), mean_3180_for
    (:), SD_3180_for(:), 'o', 'Color', [0.5, 0, 0]);
416 hFit_3180 = plot(fit_3180_for_x, fit_3180_for_y);
417 str_fit_3340 = sprintf('linear fit (y=%fx+%f)',
    fit_3340_for);
418 str_fit_3180 = sprintf('linear fit (y=%fx+%f)',
    fit_3180_for);
419 hLegend = legend([hData_3180, hFit_3180, hData_3340,
    hFit_3340], '3180 cm-1', str_fit_3180, '3340 cm
    -1', str_fit_3340, 'location', 'SouthEast');
420 hold off
421 print(fig, strcat(save_path, plot_title), '-depsc');
422
423 % Plot epi-results
424 plot_title = strsplit(save_path, '/');
425 plot_title = char(plot_title{end-1});
426 plot_title = strcat(plot_title, '-saltcalibration-', '
    epi');
427 fig = figure;
428 hold on
429 ax = gca;
430 set(ax, 'FontName', 'Helvetica');
431 hTitle = title('saltcalibration');
432 set(hTitle, 'FontSize', 12, 'FontWeight', 'bold');
433 hXLabel = xlabel('concentration of NaCl [w%]');
434 hYLabel = ylabel('intensity [a.u.]');
435 set([hXLabel, hYLabel], 'FontSize', 10);
436 set([hTitle, hXLabel, hYLabel], 'FontName', '
    AvantGarde');
437 hData_3340 = errorbar(salt_3340_epi(:), mean_3340_epi
    (:), SD_3340_epi(:), 'o', 'Color', [0, 0, 0.5]);
438 hFit_3340 = plot(fit_3340_epi_x, fit_3340_epi_y);
439 hData_3180 = errorbar(salt_3180_epi(:), mean_3180_epi
    (:), SD_3180_epi(:), 'o', 'Color', [0.5, 0, 0]);
440 hFit_3180 = plot(fit_3180_epi_x, fit_3180_epi_y);
441 str_fit_3340 = sprintf('linear fit (y=%fx+%f)',
    fit_3340_epi);
442 str_fit_3180 = sprintf('linear fit (y=%fx+%f)',
    fit_3180_epi);

```

```
443 hLegend = legend([hData_3180, hFit_3180, hData_3340,  
    hFit_3340], '3180 cm{-1}', str_fit_3180, '3340 cm{-1}',  
    str_fit_3340, 'location', 'SouthEast');  
444 hold off  
445 print(fig, strcat(save_path, plot_title), '-depsc');  
446  
447 % Save results  
448 disp('saving results');  
449 save(strcat(save_path, 'saltcalibration_results'), '  
    fit_3340_for', 'fit_3340_epi', 'fit_3180_for', '  
    fit_3180_epi');  
450 csvwrite(strcat(save_path, 'bad_data_sets.csv'),  
    bad_data_sets);  
451  
452 disp('done');
```

7.5 Script: Dataanalysis in Matlab for Calculation of Concentration of Salt in Butter

```
1 % By Brian Bjarke Jensen (brjen12@student.sdu.dk)  
    16/11-2017  
2 clearvars  
3 disp('waiting for input');  
4 show_ROIs = false;  
5 butter_density = 0.911;  
6  
7 % From most recent proper fit "170318-saltCal-epi":  
8 epi_a3340 = 0.827782;  
9 epi_b3340 = 17.951687;  
10 epi_a3180 = 0.474638;  
11 epi_b3180 = 20.976578;  
12  
13 % From most recent proper fit "170318-saltCal-for":  
14 for_a3340 = 2.614713;  
15 for_b3340 = 38.543655;  
16 for_a3180 = 1.279865;  
17 for_b3180 = 60.737177;  
18  
19 % Import and read images  
20 [filenames, path] = uigetfile('*.tif', 'Choose Images'  
    , 'MultiSelect', 'on');  
21 save_path = strsplit(path, '/');  
22 save_path = strjoin(save_path(1:end-2), '/');  
23 save_path = strcat(save_path, '/');  
24 disp('reading images');  
25 a = 1;  
26 b = 1;
```

```
27 I_info = imfinfo(strcat(path, filenames{1}));
28 for i = 1:length(filenames)
29     if contains(char(filenames{i}), '785')
30         I_3340_for{a} = imread(strcat(path, filenames{
31             i}), 1);
32         I_3340_epi{a} = imread(strcat(path, filenames{
33             i}), 2);
34         a = a + 1;
35     elseif contains(char(filenames{i}), '795')
36         I_3180_for{b} = imread(strcat(path, filenames{
37             i}), 1);
38         I_3180_epi{b} = imread(strcat(path, filenames{
39             i}), 2);
40         b = b + 1;
41     else
42         disp('ERROR: one or more filenames did not
43             meet protocol naming standard');
44         return
45     end
46 end
47 clearvars a b
48
49 % Check that images satisfy protocol standard
50 if ~exist('I_3340_for') | ~exist('I_3340_epi') | ~
51     exist('I_3180_for') | ~exist('I_3180_epi')
52     disp('ERROR: one or more image types were not
53         provided');
54     return
55 end
56 if length(I_3340_for) ~= length(I_3180_for) | length(
57     I_3340_epi) ~= length(I_3180_epi)
58     disp('ERROR: uneven number of images')
59     return
60 end
61 for i = 1:length(I_3340_for)
62     if size(I_3340_for{i}) ~= size(I_3180_for{i}) |
63         size(I_3340_epi{i}) ~= size(I_3180_epi{i})
64         disp('ERROR: one or more images are the same
65             size');
66         return
67     end
68 end
69
70 % Check that images are bright enough
71 % for i = 1:length(I_3180_for)
72 %     if mean(mean(I_3180_for{i})) < 0.035 | mean(mean
73 %         (I_3180_epi{i})) < 0.028
74 %         image_index_begin = length(filenames) / 2 +
75 %         1;
```

```
64 %         message = {'Possible error: mean intensity
    may be too low in image', filenames{
    image_index_begin + i}};
65 %         disp(strjoin(message));
66 %     end
67 %     if mean(mean(I_3340_for{i})) < 0.05 | mean(mean(
    I_3340_epi{i})) < 0.038
68 %         message = {'Possible error: mean intensity
    may be too low in image', filenames{i}};
69 %         disp(strjoin(message));
70 %     end
71 % end
72
73 % Apply noise filtering
74 disp('filtering noise');
75 p = 4;
76 for i = 1:length(I_3340_for)
77     I_3340_for{i} = filter2(fspecial('average', 4),
    I_3340_for{i}) / 255;
78     I_3340_for{i} = medfilt2(I_3340_for{i}, [p, p]);
79 end
80 for i = 1:length(I_3340_epi)
81     I_3340_epi{i} = filter2(fspecial('average', 4),
    I_3340_epi{i}) / 255;
82     I_3340_epi{i} = medfilt2(I_3340_epi{i}, [p, p]);
83 end
84 for i = 1:length(I_3180_for)
85     I_3180_for{i} = filter2(fspecial('average', 4),
    I_3180_for{i}) / 255;
86     I_3180_for{i} = medfilt2(I_3180_for{i}, [p, p]);
87 end
88 for i = 1:length(I_3180_epi)
89     I_3180_epi{i} = filter2(fspecial('average', 4),
    I_3180_epi{i}) / 255;
90     I_3180_epi{i} = medfilt2(I_3180_epi{i}, [p, p]);
91 end
92 clearvars p
93
94 % Determine regions of interest (ROIs) - using 3180-
    images as templates
95 disp('determining ROIs');
96 for i = 1:length(I_3180_for)
97     IBW_3180_for{i} = im2bw(I_3180_for{i}, graythresh(
    I_3180_for{i}));
98     ROI_3180_for{i} = regionprops(IBW_3180_for{i},
    I_3180_for{i}, {'Area', 'MeanIntensity'});
99     ROI_3180_for{i} = struct2cell(ROI_3180_for{i}).';
100    ROI_3340_for{i} = regionprops(IBW_3180_for{i},
    I_3340_for{i}, {'Area', 'MeanIntensity'});
101    ROI_3340_for{i} = struct2cell(ROI_3340_for{i}).';
```

```
102 end
103 for i = 1:length(I_3180_epi)
104     IBW_3180_epi{i} = im2bw(I_3180_epi{i}, graythresh(
105         I_3180_epi{i}));
106     ROI_3180_epi{i} = regionprops(IBW_3180_epi{i},
107         {'Area', 'MeanIntensity'});
108     ROI_3340_epi{i} = regionprops(IBW_3180_epi{i},
109         {'Area', 'MeanIntensity'});
110     ROI_3340_epi{i} = struct2cell(ROI_3340_epi{i}).';
111 end
112 clearvars IBW_3180_for IBW_3180_epi
113 % Remove bad detected ROIs
114 total_pixels = size(I_3180_for{1}, 1) * size(
115     I_3180_for{1}, 2);
116 for i = 1:length(ROI_3180_for)
117     indices = find(cell2mat(ROI_3180_for{i}(:, 1)) <=
118         4);
119     ROI_3180_for{i}(indices, :) = [];
120     ROI_3340_for{i}(indices, :) = [];
121     indices = find(cell2mat(ROI_3180_for{i}(:, 1)) >=
122         0.2 * total_pixels);
123     ROI_3180_for{i}(indices, :) = [];
124     ROI_3340_for{i}(indices, :) = [];
125 end
126 for i = 1:length(ROI_3180_epi)
127     indices = find(cell2mat(ROI_3180_epi{i}(:, 1)) <=
128         4);
129     ROI_3180_epi{i}(indices, :) = [];
130     ROI_3340_epi{i}(indices, :) = [];
131     indices = find(cell2mat(ROI_3180_epi{i}(:, 1)) >=
132         0.2 * total_pixels);
133     ROI_3180_epi{i}(indices, :) = [];
134     ROI_3340_epi{i}(indices, :) = [];
135 end
136 % OPTIONAL: Show detected ROIs on an image
137 if show_ROIs
138     i = 1;
139     imshow(I_3180_epi{i});
140     hold on
141     visboundaries(IBW_3180_epi{i});
142     hold off
143 end
144 % Calculate relative intensities (3340/3180)
145 disp('calculating relative intensities');
146 for i = 1:length(ROI_3180_for)
```

```
143     area_for_part{i} = cell2mat(ROI_3180_for{i}(:, 1))
144     ;
145     rel_for_part{i} = cell2mat(ROI_3340_for{i}(:, 2))
146     ./ cell2mat(ROI_3180_for{i}(:, 2));
147 end
148 area_for = vertcat(area_for_part{:});
149 rel_for = vertcat(rel_for_part{:});
150 clearvars area_for_part rel_for_part
151 for i = 1:length(ROI_3180_epi)
152     area_epi_part{i} = cell2mat(ROI_3180_epi{i}(:, 1))
153     ;
154     rel_epi_part{i} = cell2mat(ROI_3340_epi{i}(:, 2))
155     ./ cell2mat(ROI_3180_epi{i}(:, 2));
156 end
157 area_epi = vertcat(area_epi_part{:});
158 rel_epi = vertcat(rel_epi_part{:});
159 clearvars area_epi_part rel_epi_part
160
161 % Determine salt concentration from relative
162 % intensities
163 disp('calculating salt concentrations');
164 salt_conc_for = (for_b3180 * rel_for - for_b3340) ./ (
165     for_a3340 - for_a3180 * rel_for);
166 salt_conc_epi = (epi_b3180 * rel_epi - epi_b3340) ./ (
167     epi_a3340 - epi_a3180 * rel_epi);
168
169 % Convert areas from pixel to um^2
170 pixel_per_um = I_info(1).XResolution;
171 area_for = area_for / pixel_per_um;
172 area_epi = area_epi / pixel_per_um;
173 total_area = total_pixels / pixel_per_um * length(
174     I_3180_for);
175
176 % Calculate forward results
177 droplet_area_for = sum(area_for);
178 droplet_area_for_fraction = droplet_area_for /
179     total_area;
180 weight_for = area_for / droplet_area_for;
181 salt_conc_for_wmean = sum(salt_conc_for .* weight_for)
182     ;
183 salt_conc_for_SD = std(salt_conc_for, weight_for);
184 droplet_area_for_mean = mean(area_for);
185 droplet_area_for_SD = std(area_for);
186 sample_salt_conc_for = salt_conc_for_wmean *
187     droplet_area_for_fraction / butter_density;
188 clearvars weight_for
189
190 % Calculate epi results
191 droplet_area_epi = sum(area_epi);
```

```
181 droplet_area_epi_fraction = droplet_area_epi /
    total_area;
182 weight_epi = area_epi / droplet_area_epi;
183 salt_conc_epi_wmean = sum(salt_conc_epi .* weight_epi)
    ;
184 salt_conc_epi_SD = std(salt_conc_epi, weight_epi);
185 droplet_area_epi_mean = mean(area_epi);
186 droplet_area_epi_SD = std(area_epi);
187 sample_salt_conc_epi = salt_conc_epi_wmean *
    droplet_area_epi_fraction / butter_density;
188 clearvars weight_epi
189
190 % Save results
191 filenames = cell2mat(filenames.);
192 csvwrite(strcat(save_path, 'analysed_images.csv'),
    filenames);
193 results_table = {
194     'droplet salt concentration weighted mean [w%]:',
        salt_conc_for_wmean, salt_conc_epi_wmean;
195     'droplet salt concentration SD [w%]:',
        salt_conc_for_SD, salt_conc_epi_SD;
196     'droplet area mean [um^2]:', droplet_area_for_mean
        , droplet_area_epi_mean;
197     'droplet area SD [um^2]:', droplet_area_for_SD,
        droplet_area_epi_SD;
198     'total droplet area [um^2]:', droplet_area_for,
        droplet_area_epi;
199     'total area imaged [um^2]:', total_area,
        total_area;
200     'droplet area / total area-fraction:',
        droplet_area_for_fraction,
        droplet_area_epi_fraction;
201     'sample salt concentration [w%]:',
        sample_salt_conc_for, sample_salt_conc_epi};
202 results_table = cell2table(results_table, '
    VariableNames', {'result', 'forward', '
    epifluorescent '});
203 writetable(results_table, strcat(save_path, 'results.
    txt'));
204
205 % Determine plot size-limits
206 x_limit_for_max = max(area_for) * 2;
207 x_limit_epi_max = max(area_epi) * 2;
208 y_limit_for_min = min(salt_conc_for) * 1.1;
209 y_limit_for_max = max(salt_conc_for) * 1.1;
210 y_limit_epi_min = min(salt_conc_epi) * 1.1;
211 y_limit_epi_max = max(salt_conc_epi) * 1.1;
212 x_limit_min = 0;
213 if x_limit_for_max > x_limit_epi_max
214     x_limit_max = x_limit_for_max;
```

```
215 else
216     x_limit_max = x_limit_epi_max;
217 end
218 if y_limit_for_min < y_limit_epi_min
219     y_limit_min = y_limit_for_min;
220 else
221     y_limit_min = y_limit_epi_min;
222 end
223 if y_limit_for_max > y_limit_epi_max
224     y_limit_max = y_limit_for_max;
225 else
226     y_limit_max = y_limit_epi_max;
227 end
228 clearvars x_limit_for_max x_limit_epi_max
        y_limit_for_min y_limit_for_max y_limit_epi_min
        y_limit_epi_max
229
230 % Plot forward-detected results
231 disp('plotting results');
232 path = strsplit(save_path, '/');
233 fig = figure;
234 hold on
235 ax = gca;
236 ax.XScale = 'log';
237 xlim([x_limit_min, x_limit_max]);
238 ylim([y_limit_min, y_limit_max]);
239 set(ax, 'FontName', 'Helvetica');
240 hTitle = title(strcat(path{end-2}, '-for'));
241 set(hTitle, 'FontSize', 14, 'FontWeight', 'bold');
242 hXLabel = xlabel('size [um2]');
243 hYLabel = ylabel('conc. of NaCl [w%]');
244 set([hXLabel, hYLabel], 'FontSize', 12);
245 set([hTitle, hXLabel, hYLabel], 'FontName', '
        AvantGarde');
246 hData = plot(area_for, salt_conc_for, 'o', 'Color',
        [0,0,0.5]);
247 print(fig, strcat(save_path, path{end-2}, '-', path{
        end-1}, '-for'), '-depsc');
248 hold off
249
250 % Plot epi-detected results
251 fig = figure;
252 hold on
253 ax = gca;
254 ax.XScale = 'log';
255 xlim([x_limit_min, x_limit_max]);
256 ylim([y_limit_min, y_limit_max]);
257 set(ax, 'FontName', 'Helvetica');
258 hTitle = title(strcat(path{end-2}, '-epi'));
259 set(hTitle, 'FontSize', 14, 'FontWeight', 'bold');
```

```
260 hXLabel = xlabel('size [um2]');
261 hYLabel = ylabel('conc. of NaCl [w%]');
262 set([hXLabel, hYLabel], 'FontSize', 12);
263 set([hTitle, hXLabel, hYLabel], 'FontName', '
    AvantGarde');
264 hData = plot(area_epi, salt_conc_epi, 'o', 'Color',
    [0,0,0.5]);
265 print(fig, strcat(save_path, path{end-2}, '-', path{
    end-1}, '-epi'), '-depsc');
266 hold off
267 clearvars x_limit_min x_limit_max y_limit_min
    y_limit_max
268
269 disp('done');
```